

XSGRB - The X-shooter GRB afterglow sample [★]

J. Selsing¹ and XSGRB collaboration

Dark Cosmology Centre, Niels Bohr Institute, University of Copenhagen, Juliane Maries Vej 30, 2100 København Ø, Denmark

Received/ accepted

ABSTRACT

In this work we present the spectra of *all* γ -ray bursts (GRBs) afterglows that have *ever* been observed at the VLT/X-shooter up to the end of 2016. This totals 137 spectroscopic observation of 118 individual bursts, of which redshifts have been secured for 91 % covering a redshift range from 0.059 to ~ 8.5 . Based on a set of unbiasing selection criteria, the follow-up effort has been guided by the *Swift*-telescope to produce a homogeneous sample of afterglows for 86 spectra, representing the underlying *Swift* GRB population. We here provide a public release of all the spectra, including continuum estimates and telluric corrections. We provide an assessment of the degree of completeness with respect to the parent GRB population, in terms of the X-ray properties of the bursts in the sample and find that the sample presented here can not be significantly distinguished from the *Swift* sample. For all bursts (39) for which it is possible, we provide a measurement of the optically derived hydrogen column density, increasing the total number of published HI column densities by ~ 50 % and characterize the distribution compared with literature values. We constrain the fraction of dark burst to be 27% - 42% (**Preliminary**) and tentatively confirm previous results that larger optical darkness leads to increased X-ray absorption.

Key words. Gamma-ray burst: individual: GRB 120815A — galaxies: high-redshift — ISM: molecules — dust, extinction

1. Introduction

For a brief moment, the energy output of a γ -ray burst (GRB) can rival that of the stellar light integrated over the entirety of the observable universe (Kumar & Zhang 2015). Bright across the entire electromagnetic spectrum, the following afterglow makes possible the exploration of the intervening space, otherwise dark. Since the discovery of the first γ -ray counterparts nearly two decades ago (Costa et al. 1997; van Paradijs et al. 1997; Djorgovski et al. 1997; Frail et al. 1997; Wijers et al. 1998), significant advances in the understanding of the underlying phenomenology and potential usage has been made.

Categorized on the basis of their duration and spectral hardness, two main classes of GRBs exist, long and short (Kouveliotou et al. 1993). Now thoroughly established, the connection between long GRBs and supernovae (SNe) (Galama et al. 1998; Hjorth et al. 2003; Stanek et al. 2003; Woosley & Bloom 2006) and the association of the location of long GRBs with the most star-forming regions in their host galaxies (Fruchter et al. 2006; Svensson et al. 2010), make a stellar origin a likely explanation for the progenitor system. The seeming metal aversion (Graham & Fruchter 2013; Krühler et al. 2015; Perley et al. 2016b) in selection of host at low redshift along with theoretical single-progenitor models preferring more pristine starting conditions (Woosley & Heger 2006), paints a picture where the core of a rapidly spinning, massive star undergoes gravitational collapse, although a certain degree of binarity (Fryer & Heger 2005; Podsiadlowski et al. 2010) in the progenitor population is required to explain the host metallicity distribution to super solar values

(Niino 2011), see Levan et al. (2016) for recent review. The driving engine in short GRBs has been established as the merger of two compact objects (Metzger et al. 2010) through the detection of an associated kilonova (Tanvir et al. 2013; Berger et al. 2013). With the advent of the first gravitational wave (GW) detection Abbott et al. (2016), the electromagnetic counterpart in the form of a short

GRBs as cosmological probes
 Do GRBs trace star formation
 Afterglow spectroscopy
 Complete samples

Only after observing more than 12000 damped Lyman- α absorbers (DLAs) towards about 10^5 QSOs have 5 systems with $\log(N_{\text{HI}}/\text{cm}^{-2}) > 22$ been identified (Noterdaeme et al. 2012). Long GRB afterglow spectra, by contrast, reveal such systems in the majority of cases (Jakobsson et al. 2006b; Fynbo et al. 2009). Whereas DLAs towards QSOs are mostly limited to $1.8 \lesssim z \lesssim 5$ due to the atmospheric UV-cutoff and increasing Lyman-blanketing at increasing redshifts (e.g., Rafelski et al. 2014), GRBs allow us to see into the hearts of star-forming galaxies over the full history of cosmic star formation from $z \approx 0$ to $z > 8$ (e.g., Tanvir et al. 2009; Salvaterra et al. 2009; Jakobsson et al. 2012). With afterglow spectroscopy (throughout the electromagnetic spectrum from X-rays to the sub-mm) we can hence characterize the properties of star-forming galaxies over cosmic history in terms of redshifts, metallicities, molecular contents, ISM temperatures, UV-flux densities.

Content of paper

2. Sample selection criteria and follow-up

2.1. Sample selection criteria

Being of transient nature, it is difficult to impose strong sample selection criteria on GRBs, without hampering the follow-up

[★] Based on observations collected at the European Southern Observatory, Paranal, Chile, Program ID: 098.A-0055, 097.A-0036, 096.A-0079, 095.B-0811(B), 095.A-0045, 094.A-0134, 093.A-0069, 092.A-0124, 0091.C-0934, 090.A-0088, 089.A-0067, 088.A-0051, 087.A-0055, 086.A-0073, 085.A-0009 and 084.A-0260

effort. Many natural follow-up restrictions exist already, being it weather conditions, pointing restrictions of the telescope or poorly localized bursts as reported by the alerting telescope. To maximize the return of the follow-up campaign we have chosen a few selection criteria that attempt to provide an unbiased selection of bursts, while allowing for a high follow-up success rate. The importance of defining unbiased selection criteria has been highlighted previously (Salvaterra et al. 2012; Hjorth et al. 2012; Vergani et al. 2015; Perley et al. 2016a), when trying to address the specific underlying distribution functions such as the redshift distribution, host metallicity distribution, or brightness distribution. When investigating a specific distribution function, a high degree of *completeness* is desired meaning that in terms of the parameter of interest, the largest possible fraction of targets in the sample has determinations of that parameter (Perley et al. 2016b).

We simultaneously want to minimize any biases against astrophysical conditions while at the same time maximizing likelihood of observations allowing us to obtain a higher degree of observing completeness. By restricting the selection criteria to conditions local to Galaxy and therefore irrespective of intrinsic GRB properties, the hope is that the sample collected represents the underlying distribution of GRBs in a fair way while at the same time, additional unbiasing cuts can be imposed that can improve the follow-up success. The selection criteria used here is based on previous successes Jakobsson et al. (2006a); Fynbo et al. (2009); Hjorth et al. (2012), which has shown to represent the underlying distribution to a high degree. We test the degree of completeness in Sect. 5.2.

The selection criteria are defined as follows:

1. GRB triggered onboard by Swift.
2. XRT started observing within 10 minutes since the GRB; an XRT position must be distributed within 12 hr.
3. The target must be visible for at least 60 minutes at least 30 degrees above the horizon, with the Sun below -12° .¹
4. No bright nearby stars.
5. Galactic $A_V \lesssim 0.5$ mag.

Because our ability to observe GRB afterglows is strongly correlated with the rapidness and precision of the target positions delivered by the triggering facilities, by selecting only bursts that have been triggered on board the *Swift* space telescope Gehrels et al. (2004), by the Burst Alert Telescope (BAT) (Barthelmy et al. 2005), we start out with a homogeneously selected sample where burst characteristics are delivered immediately, allowing for an informed follow-up strategy. Despite the complexity of the triggering mechanism on board *Swift* (Band 2006), attempts at inferring properties of the underlying cosmic GRB population based on the detection thresholds and triggering algorithms have been made (Lien et al. 2014; Graff et al. 2016) and thereby by restricting the follow-up effort to bursts detected by *Swift*, the limitations of the parent sample is well studied.

Because the localization accuracy of BAT is 1 - 4 arcminutes (Barthelmy et al. 2005), we additionally require an X-ray position from the X-ray Telescope (XRT) (Burrows et al. 2005) to be distributed to the GCN network (Barthelmy 2000) with 10 hours and to account for observing constraints on *Swift* that XRT began observations within 10 minutes. The additional rapidness

requirement of the XRT follow-up means that the number of detected X-ray afterglows for BAT triggers is 100 percent (Burrows et al. 2007). The *Swift* constraints on the GRB follow-up means that the sample presented here inherits the *Swift* sample properties, except the additional XRT constraint. Because the XRT completeness is very high (Burrows et al. 2007), this should change the parent sample significantly. This issue is addressed again in Sect. 5.2.

To allow for observability we additionally require that the GRB is visible (duh!) from the telescope site at Cerro Paranal, Antofagasta, Región de Antofagasta, Chile, for at least 1 hour allowing time for the spectroscopic observations to be completed. Since the GRB population is isotropically distributed seen from Earth and that GRB properties do not depend on position on the sky (Briggs et al. 1996), this cut does not influence our ability to sample the underlying GRB population. The same arguments apply to the requirement that there are no nearby bright stars, which is additionally supplemented by the requirement that the galactic dust content does not exert an extinction higher than $A_V \lesssim 0.5$ mag based on the extinction maps by Schlegel et al. (1998). Because of isotropy, these additional cuts should not influence the optical properties of the bursts themselves, only our ability to successfully secure observations that allows us to investigate the spectroscopic properties of GRBs.

We address the successfulness of these criteria and the actual follow-up effort in representing the full *Swift* sample in Sect. 5.2.

2.2. Follow-up procedure and practicalities

(Will be written by Daniele?)

2.2.1. RRM observations

The rapid-response mode is

3. Observations

Observations in this sample have been carried out using the cross-dispersed echelle spectrograph, X-shooter (Vernet et al. 2011), mounted on two of the four Unit Telescopes at ESO/VLT, UT2 (Kueyen) and UT3 (Melipal) during the duration of this follow-up campaign, which covers the entire lifetime of X-shooter. Observations have been carried out from the ESO period P84 through P98 under the following programme IDs: 098.A-0055, 097.A-0036, 096.A-0079, 095.A-0045, 094.A-0134, 093.A-0069, 092.A-0124, 0091.C-0934, 090.A-0088, 089.A-0067, 088.A-0051, 087.A-0055, 086.A-0073, 085.A-0009 and 084.A-0260. A few additional bursts, not a part of the *statistical sample*, have been included from 092.D-0056(A) (PI: Rau), 092.D-0633(E) (PI: Greiner), and Levan under 095.B-0811(B) (PI: Levan). This sample represents *all* GRBs that have ever been followed up by X-shooter.

The first GRB followed up is GRB090313, observed 15th of March 2009, which was while X-shooter was mounted on UT3 during the commissioning of the instrument. The bursts observed during the commissioning period are not a part of our statistical sample, but are nonetheless published as part of the bursts observed by the X-shooter GRB team. The first burst observed after science verification was completed when X-shooter was moved to UT2 is GRB091018 which thereby constitutes the first burst entering our statistical sample. For all bursts that fulfill our sample selection criteria, described in Sect. 2.1, spectroscopic follow-

¹ Note that in the P84 proposal the criteria have been stated a bit differently, the visibility constraint being replaced by a declination + Sun angle constraint. The below criteria are however those defining the sample.

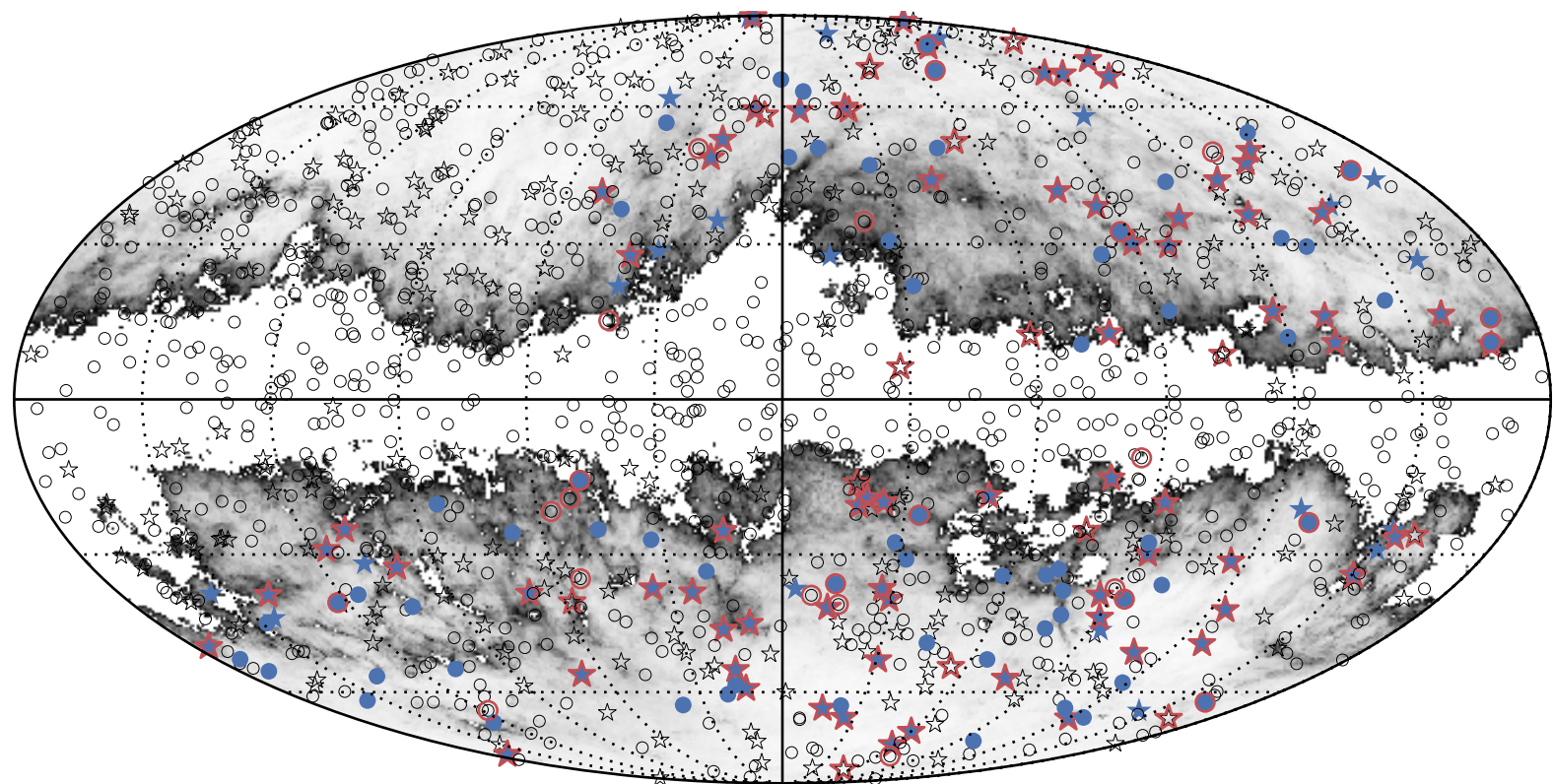


Fig. 1: Mollweide projection in galactic coordinates of the full sky showing the positions on the sky of the bursts presented in this work. The empty circles are the positions of all the *Swift* bursts detected until the end of 2016. In blue is shown the position of the bursts fulfilling the sample criteria specified in Sect. 2.1. The red circles are added around GRBs which have been followed up by X-shooter since the commissioning of the instrument. Blue points with red circles represent GRBs that enter our sample and have X-shooter spectroscopy. The different samples are compared in Sect. 5. The background shows the dust maps presented in Schlegel et al. (1998) where the sample criteria cut with $A_V \lesssim 0.5$ mag is removed.

up has been attempted with X-shooter. Various conditions can affect our ability to follow up a given burst, and a discussion of this effect is included in Sect. 5.3.

X-shooter can cover the spectral wavelength region from 3000 Å to 24800 Å in a single exposure, by splitting the light in three separate spectroscopic arms using dichroics. This way each arm work as a separate instrument, each functioning as its own echelle spectrograph. The ultraviolet blue(UVB) arm covering 3000 - 5500 Å, the visual(VIS) arm covering 5500 - 10200 Å, and the near-infrared(NIR) arm covering 10200 - 24800 Å with the possibility of applying a k-band blocking filter cutting the coverage of the NIR arm at 10200 - 21000 Å.

(ABBA)

For the large majority of the bursts we have observed with a slit width of 1'0, 0'9, and 0'9 for the UVB, VIS, and NIR-arm respectively, which puts a lower limit on the delivered resolution of the spectra based on the tabulated values of the delivered resolutions, which is 4350, 7450, and 5300 for the UVB, VIS and

NIR-arm respectively². The slit width also sets the width of the atmospheric sky lines and determines the amount of light lost due to the wavelength-dependent seeing PSF extending outside the coverage of the slit, where the width of sky-lines is always set by the slit width whereas both the delivered resolution and the slitloss changes for the better as the seeing PSF drops below the slit width. For atmospheric conditions delivering a seeing PSF with a FWHM of 0'9 observed with a 0'9 slit only 76.1 percent of the light will enter the slit, meaning that for almost all observations a slitloss correction is required. We describe how slit-losses were corrected for in Sect. 4.1. For accurate measurements of velocity widths, a precise instrumental resolution is required and this becomes better when the delivered seeing is better than the slit width. We discuss this in Sect. 4.5.

(ADC discussion)

We list the overview of all the observations in Tab. 1. and plot the positions off all the bursts on the night sky in Fig. 1. The

² <https://www.eso.org/sci/facilities/paranal/instruments/xshooter/inst.html>

central zone of avoidance due to high galactic extinction cutoff is visible with an apparent isotropic distribution of the bursts away from the galactic center except in the upper right corner, where Earth casts a shadow on the sky as seen from the telescope.

4. Data processing

In this section we describe how the final data products are produced and subsequently post-processed. ~ 30 percent of the data released here have been reduced in a manner similar to what is described in Krühler et al. (2015). The two reduction schemes have been tested and are in good agreement. All post-processing scripts developed for this dataset are made publicly available at https://github.com/jselsing/XSGRB_reduction_scripts, along with instructions of use.

Before any reductions are done, the raw object images are run through the cosmic-ray removal algorithm (van Dokkum 2001) implementation, *Astro-SCRAPPY*³, where a wide clipping radius have been used around detected cosmics to ensure that edge residuals are robustly rejected.

The basis for the reductions is the VLT/X-shooter pipeline, version 2.7.1 or newer (Goldoni et al. 2006; Modigliani et al. 2010). The pipeline is managed with the Reflex interface (Freudling et al. 2013) and is used for subtraction of bias level, flat-fielding, tracing of the echelle orders, wavelength calibrations with the use of arc-line lamps, flux calibration using spectrophotometric standards (Vernet et al. 2009; Hamuy et al. 1994), mirror flexure compensation, initial sky-subtraction and lastly the rectification and merging of the orders. For the initial sky-subtraction, the background has been estimated in regions adjacent to the object trace clear of contaminating sources. Because of the broken ADC, for some objects there is a lot of curvature in the object trace. This means that for some bursts, the initial sky-estimate has been made from a limited number of pixels in the spatial direction. By doing an initial subtracting the sky on the un-rectified image we ensure that bulk of the sky background is not redistributed by the rectification process.

The image is rectified onto an equidistant grid with a dispersion sampling of 0.2 \AA/pixel and a $0.16''/\text{pixel}$ spatial sampling for the UVB and VIS arm and 0.6 \AA/pixel with a $0.21''/\text{pixel}$ in the NIR arm. Because the tabulated resolution is a lower limit, by choosing a sampling of 0.2 \AA/pixel , we ensure that the bluest part of neither of the arms have a sampling lower than the Nyquist sampling rate of 2 pixels per resolution FWHM.

4.1. Post-processing

For a typical observation, each of the exposures in the nodding sequence has been reduced as single observation and then subsequently combined to form a single image. Because this strategy is employed, we can reject outliers in the stack and weight by the average inverse variance of the background. When weighting images where the noise in each pixel is dominated by Poisson noise it is important to estimate the background variance in a large enough region, so that to remove the correlation between the signal and the weights. To this end, the weight map is generated by a running median window over the variance map, where the trace has been masked and width of the window is chosen to be wide enough for median variance to be generated on the basis of several hundred pixels. This weighting scheme automatically also optimally combines images of different exposure times or

images where the background is varying, which is often the case when a burst has been observed close to twilight

Because the background is very bright and there is a high abundance of broad sky-lines in the NIR arm, when there are no contaminating sources in the slit, the sky has been put back on the images and they have been reduced in pairs of two, subtracting the two from each other, keeping the WCS static. This amounts to the regular nodding reduction, only we can reject outliers and weight by the averaged inverse variance map.

By STARE reducing all observations we additionally get a spectrum of the sky, which we can use to calibrate the wavelength solution in Sect. 4.2.

4.2. Correction for offsets in the wavelength calibration

X-shooter, being installed at the VLT Cassegrain focus is prone to flexures during operations. The flexures modify the projection of the slit on the detector with respect to the one obtained in day-time calibration. This requires a modification of the wavelength solution in order to process correctly the night-time data. Part of this correction is performed by the pipeline using the frames taken during X-shooter Active Flexure Compensation procedure⁴.

The remaining offset is corrected by cross-correlation with a synthetic sky spectrum (Noll et al. 2012; Jones et al. 2013) after the continuum, estimated as the mode of all flux values, has been subtracted. To get the correct seeing PSF with which to convolve the synthetic sky an initial refinement of the wavelength solution have been obtained by cross-correlating the observed sky with an unconvolved synthetic sky. This preliminary wavelength calibration is applied to the observed sky. The synthetic spectrum is then convolved with an increasing seeing PSF and the width that minimizes χ^2 with the updated observed sky is chosen to be the effective sky-PSF. Using the synthetic sky with the matched resolution, a final wavelength calibration can then be calculated by cross-correlating the observed sky with the correctly broadened sky spectrum, as a function of a velocity offset. Both a multiplicative and an additive offset to the wavelength calibration has been tested, but in terms of χ^2 , the model with only a multiplicative offset is preferred.

The resulting offsets, which were smaller than 0.1 \AA in the UVB and VIS data and smaller than 0.5 \AA in the NIR spectra, but changing over short period of time were applied to the corresponding spectra.

Using the convolved synthetic sky, the $\geq 3\sigma$ sky brightness pixels have been added to the bad pixel map to avoid the cores of the brightest sky-lines.

4.3. Spectral extraction

To extract the afterglow spectrum from the rectified 2D-image, several techniques have been employed based on the brightness of the afterglow and the complexity of the objects entering the slit. Due to the malfunctioning ADC, see Sect. 3, the spectral trace moves across the slit as a function of wavelength for a large fraction of the bursts observed meaning that using a single aperture for the spectral extraction is inadequate due to the large amount of background that would then enter the slit. To optimally select the extraction regions we therefore need to model the trace position.

³ <https://github.com/astropy/astrocrappy>

⁴ X-shooter User Manual available at <https://www.eso.org/sci/facilities/paranal/instruments/xshooter/doc.html>

To get the shape and the position of the spectral PSF as a function of location on the image, we need to choose a model which can represent how the light falls on the slit. We know from Trujillo et al. (2001) that the Moffat function (Moffat 1969) adequately describes an imaging PSF due to atmospheric turbulence, but due to the aberrations in the dispersion elements and the rectification process, the PSF we are trying to model differs from this profile. To allow for flexibility in the model, we have chosen the Voigt function as a model for the spectral PSF and we describe how this is evaluated in App. A. Since additionally, the host galaxy could also have a contribution to the image profile, this choice allows for the required freedom if additional flux is in the wings of the profile.

To guide the guess position of the trace on the slit as a function of wavelength, we have used the analytic prescription for the trace position described in Filippenko (1982), where the header keywords of the observations have been queried for the ambient conditions which controls the degree to which the trace moves.

Based on the signal-to-noise of the afterglow continuum, the 2D-image has been binned down in the spectral direction to a number of elements that allows for an accurate tracing of the PSF, typically 200 bins for moderate signal-to-noise. For each of the bins and using the guess position, the spectral PSF has been fit using the unweighted chi-squared minimization algorithm implemented in `scipy.optimize.curve_fit` (Jones et al. 2001). Since we know that the trace varies slowly as a function of wavelength, we have then fitted a low-order polynomial to the fit parameters as a function of wavelength, which allows us to evaluate the spectral PSF at all wavelengths and this way accurately model the entire spectral PSF.

Equipped with a model for how the light falls on the entire image, we can then employ the optimal extraction algorithm Horne (1986), which weights the extraction aperture by the spectral profile, or alternatively sum all pixels within 1 FWHM of the modeled profile. Where possible, we have used the optimal extraction. In cases where the trace is very weak, even in the binned images, an aperture has been selected manually which covers emission lines, if present, and when nothing is immediately visible, the entire nodding window. The error- and bad pixel maps are in all cases propagated throughout the extraction.

In cases where multiple traces are visible in the slit, additional components for the profile are used in the optimal extraction. The additional components do not share the PSF parameters and in cases where the additional component is an extended object, the fits have been inspected to ensure that the additional component does not skew the fit towards a different PSF. The additional components are not used for the weights.

The spectra are corrected for galactic extinction using the $E(B-V)$ value from the dust maps of Schlegel et al. (1998) with the update in Schlafly & Finkbeiner (2011)⁵, and the extinction curve by Cardelli et al. (1989) with a total to selective extinction $R_V = 3.1$. The wavelengths of the extracted 1D-spectra are moved to vacuum, moved to the barycentric frame, and the wavelength recalibration described in Sect. 4.2 is applied. Pixels with pixel-to-pixel variation large than 50σ are added to the bad pixel map.

4.4. Telluric correction

For all earth-based telescopes, the light of interest has to pass through Earth's atmosphere, where the atmospheric content and

conditions make an imprint on the received spectrum. These telluric features can be corrected for in a multitude of ways. We employ a prioritized list of methods here, depending on the availability of the different method. Since the observation is often taken at odd times under varying conditions, this prioritized list ensures that we are always doing the optimal correction.

The highest priority method is using the GRB afterglow continuum itself, where the atmospheric conditions have directly been imprinted on the spectrum. The telluric features can directly be fit with an atmospheric model (Smette et al. 2015; Kausch et al. 2015), which can then be used to correct for the absorption. The accuracy of the correction depends on the S/N for the target spectrum, where we have chosen the requirement that the afterglow continuum spectrum has a median signal-to-noise higher than a value of 10.

If the afterglow is not sufficiently bright, telluric standard stars observed close in time to the GRB can be used as a proxy for the atmospheric condition during the GRB observation. Here we employ the telluric correction method that has been developed in Selsing et al. (2015), where a library of synthetic templates is fit to the observed telluric standard.

In the last case, where the object is neither bright enough, or there for some reason have not been observed a telluric standard, we rely on the synthetic sky model by (Noll et al. 2012; Jones et al. 2013) for which we generate a synthetic transmission spectrum, which we then use, where the ambient parameters for the observations have been used.

4.5. Spectral resolution

The afterglow spectra described in this paper are obtained in Target-of-Opportunity (override) mode. In most cases there is therefore little possibility to tweak slit widths to the seeing at the time of observations (i.e. to optimise spectral resolution and signal to noise), and almost all our data is therefore taken with a fixed set of slit widths and binning, described above. In a fair number of cases, the seeing full width at half maximum (FWHM) is considerably smaller than the slit width, and the delivered spectral resolution will then be determined by the seeing rather than slit width, as afterglows are point sources (this is evidently not the case for extended sources, e.g. for host galaxies). The delivered resolution for slit width dominated spectra post-reduction and extraction can easily be determined from the bright sky emission lines. For afterglow spectra with very high signal to noise, the delivered spectral resolution can at times be determined from the science data themselves. However, in the presence of multiple velocity components in absorption, other forms of line broadening, and a lack of lines at some redshifts, this is difficult to do at poorer signal to noise ratios (the majority of spectra in our sample). A broad starting value for the expected resolution will help fitting of these spectra, and can be important in upper limit determination, and for this reason we construct a aim to construct a crude relation between the seeing and the delivered resolution at our slit width, binning, and reduction pipeline settings. To this end we use observations of telluric standard stars that are taken with identical instrument settings as our afterglow spectra, usually just after the science data, as part of the ESO X-shooter calibration plan. These spectra have been reduced together with the afterglow spectra, using identical pipeline settings with the same version of the pipeline. First we fit a Gaussian function in the spatial direction of the trace of the standard star at 792 nm (i.e. in the VIS arm). After this, we fit a series of 20 telluric absorption lines in the telluric standard star spectra with Gaussians, taking care to select transitions that

⁵ Queried from <http://irsa.ipac.caltech.edu/applications/DUST/index.html> using Ginsburg et al. (2016)

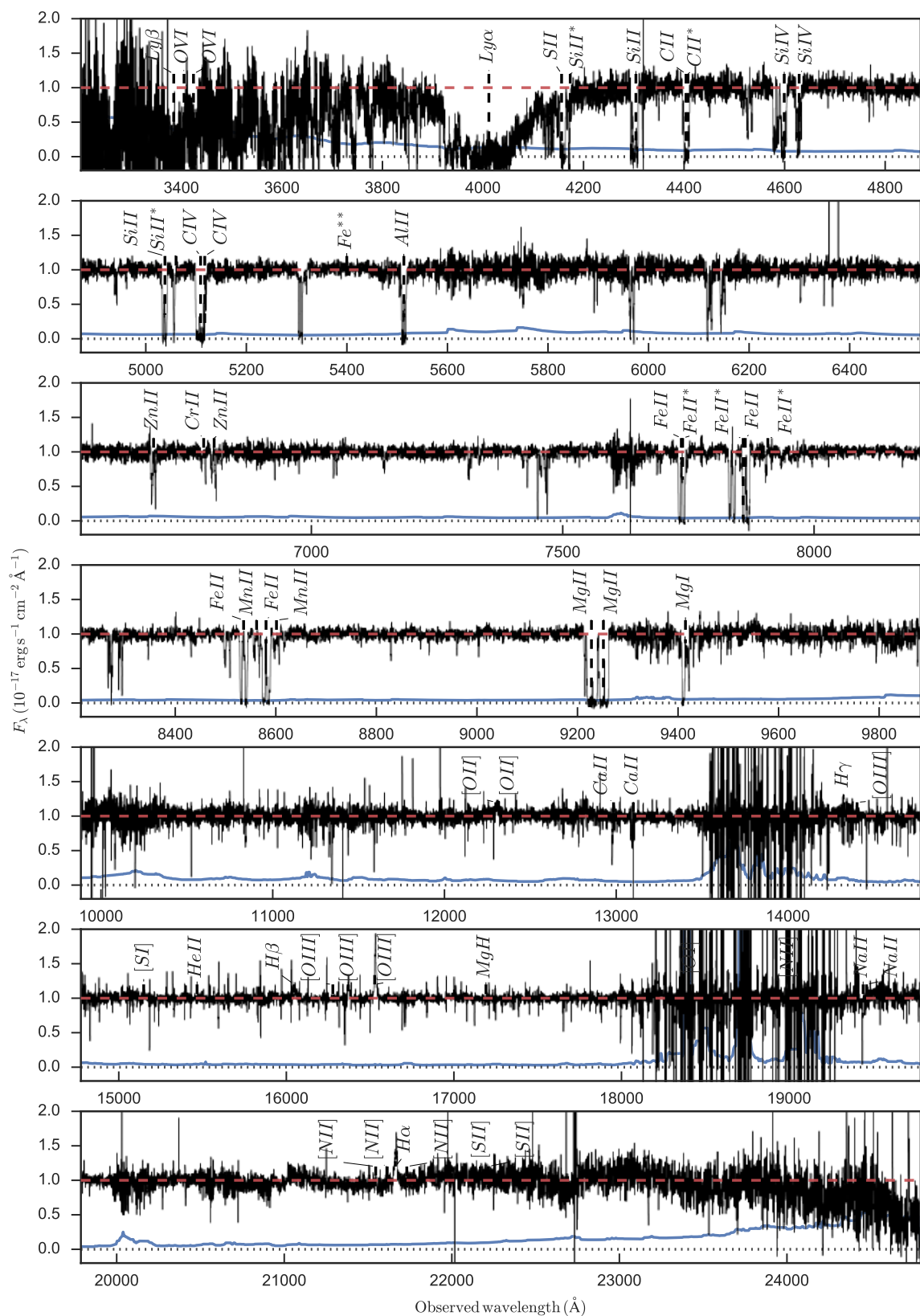


Fig. 2: Telluric corrected, normalized spectrum of GRB121024A at $z = 2.300$, meant to illustrate the typical data quality. The acquisition magnitude is $r = 20$, meaning it is in the brighter end of the sample presented here, but not the brightest. The spectrum is rich in absorption, including molecular absorption of H_2 . The absorption trough visible at $\sim 4000 \text{ \AA}$ is due to Ly α in the host. We have overplot the most prominent lines seen in GRB afterglows from Christensen et al. (2011). The continuum estimate is shown in dashed red. Additionally, three intervening systems are seen in this sightline This spectrum has been analyzed in detail in Friis et al. (2015).

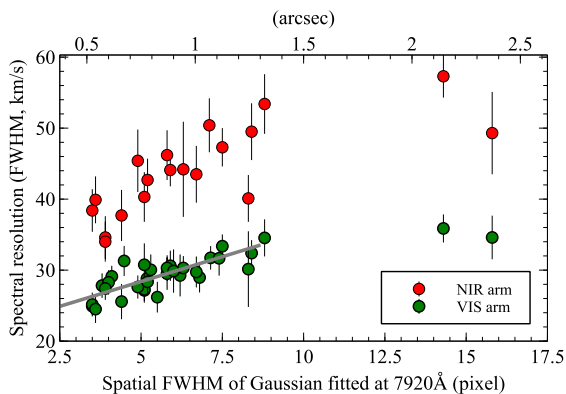


Fig. 3: Green datapoints show the FWHM (km/s) of Gaussian fits to unresolved telluric absorption lines in the VIS spectra, as a function of the FWHM of a Gaussian fit onto the trace in spatial direction at 792 nm. The lower horizontal axis is in units pixels, the top axis in arc seconds. The red datapoints show a subsample of NIR spectra. The grey line shows a linear fit to the VIS datapoints.

are not almost-resolved multiples, should be intrinsically unresolved, and are in areas with well defined continuum flux. We pick 34 telluric standard stars spanning a range of DIMM seeing values, with the majority between $0.5 - 1.5 \text{ arcsec}$. The resulting distribution of spectral FWHM (km/s) as a function of spatial FWHM at 792 nm is fairly well described by a linear relation $a + b * x$, with x the spatial FWHM in pixels (with 0.15 arc sec per pixel), $a = 21.4 \pm 1.3 \text{ km/s}$, $b = 1.4 \pm 0.2$. We use this linear relation as a way to estimate the spectral resolution for medium to poor signal to noise afterglow spectra in the VIS arm. To extend this to the UVB and NIR arm, we measured a series of lines in NIR arm spectra of a subset of 19 sources used for the VIS arm above, and find that the resulting distribution is consistent with a simple scaling of the VIS arm relation by the ratio of resolutions of the NIR and VIS arm for unresolved, slit filling, sources as given on the ESO instrument website. The UVB arm contains no suitable absorption lines to use, and we therefore use a scaled value as in the NIR arm. While this simple method is not terribly accurate (for one, the spatial profile of the trace is not a perfect Gaussian), but it gives a sufficiently accurate estimate for the analysis of these poor signal to noise science spectra.

4.6. Science data products

In this section we describe the data format. Similar to what is done in [Lopez et al. \(2016\)](#)

5. Results

In this section we describe the efficiency of the follow-up effort and the characteristics of the observed bursts. We also assess the degree to which the sample obtained is complete. An important note is that here we present *all* GRBs that have ever been observed with X-shooter, while only a subset of these constitute our *statistical* sample. The statistical sample is based on the selection criteria described in Sect. 2.1 and should represent an unbiased sample of the underlying, parent GRB population. Single bursts outside the sample criteria have been followed up on the basis of the curiosity of their light curve or their brightness, but is not discussed as part of the investigation of the GRB popula-

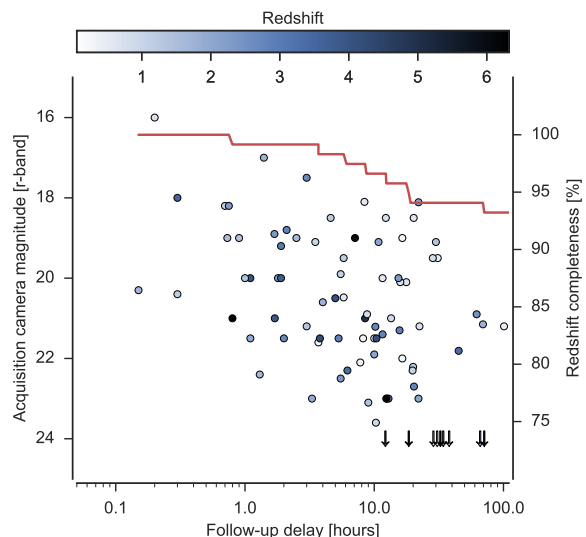


Fig. 4: Follow-up timing and afterglow magnitude at the start of observation. The points have been colored based on the redshift of the corresponding burst. Points with black faces does not have a redshift determination and downarrows indicate a non-detection in the acquisition image. In blue is shown the fractional redshift completeness as a function of delay-time.

tion. A prime example of a burst outside the statistical sample is GRB161023A with its rich spectrum containing 11 intervening absorption systems and pending further analysis.

5.1. Follow-up timing and afterglow brightness

Redshift determination of bursts where the host is too faint for a spectroscopic redshift relies on the absorption spectrum imprinted on the GRB afterglow continuum, which again depends on the afterglow brightness at time of follow-up. Because the afterglow rapidly fades ([Nousek et al. 2006](#); [Vecchio et al. 2016](#)) (**Better references**) a rapid follow-up is essential for the accurate designation of the GRB host (**Get reference**). In Fig. 4 we plot the follow-up delay from the BAT trigger to the start of the spectroscopic observation. Visible as the shortest delays are the bursts observed in RRM-mode in which where the fastest follow-up between BAT trigger and start of spectroscopic observations is for the short, $z = 1.717$, GRB160410A which was followed up only 8.4 minutes after the BAT trigger.

To illustrate the effect of redshift completeness loss due to late follow-up, we overplot the redshift completeness fraction over the delay time. Visible is the increasing fraction of GRBs without a good redshift determination for increasing delays. That the redshift completeness of the bursts we have followed up are > 90 percent (**Get number**), shows the ability of VLT/X-shooter to successfully get redshifts. Not shown in the figure is an additional 12 (**Get number**) bursts that we have redshift determinations from late-time host observations with delay-times longer than ~ 10 days.

5.2. Sample completeness

Based on the sample criteria specified in Sect. 2.1, a total of 158 (**Get number**) bursts has been triggered by *Swift* in the period

since the commissioning of VLT/X-shooter in November, 2009. This sample constitutes the *statistical sample* on which we will try to address the GRB population properties. Of this sample, 86 (**Get number**) have been spectroscopically followed up with X-shooter. In order to assess whether our sample criteria and the subset of bursts followed up represent the underlying parent population of GRB, we compare some intrinsic GRB properties of our sample to the full sample of GRBs followed up by *Swift*. Under the assumption that *Swift* randomly samples the underlying GRB population, if the sample statistics of our subsample are similar to the *Swift*-sample, we can assume that the population properties should be conserved. There is some evidence that the burst duration does not scale with redshift as expected through time-dilation (Kocevski & Petrosian 2013; Littlejohns et al. 2013), pointing towards that we could be missing an increasing fraction of the bursts at higher redshifts, but Lien et al. (2016) argues that we should only be missing the bright "short" GRBs", but to the degree that *Swift* is complete, we can test if the sample presented here is complete. We show the comparison between the burst properties in Fig. 5.

Using the observational characteristics of the 1244 (**Get number**) bursts observed by *Swift* to date Gehrels et al. (2009), and the X-ray derived hydrogen column densities (Evans et al. 2009), we can quantify the degree to which our sample is biased against the overall *Swift* sample in terms of intrinsic GRB properties. The values are queried from the online *Swift* database maintained⁶. Three main samples are of interest to compare to assess the completeness of the follow-up campaign; the full *Swift* sample consisting of all the bursts observed by *Swift*, excluding the bursts entering our sample (1), the burst that fulfill the selection criteria imposed in Sect. 2.1, but has not been followed up (2), and the bursts actually followed up with X-shooter (3).

For each of the samples we calculate the median and 14th and 86th percentile which can be used as point estimates for the population distribution. These are shown in 2. It can be seen from the values that the three samples have very similar distributions in terms of the point estimates chosen, suggesting that our selection criteria are unbiased against the *Swift*-sample and that additionally, the follow-up effort is unbiased towards the intrinsic GRB properties. This is despite spectroscopic follow-up only being carried out in cases where either a detectable optical afterglow or a clear counterpart are seen, which naively should be biased against dark bursts occurring in more obscured galaxies, which is shown to exhibit different galactic properties (Perley et al. 2009; Krühler et al. 2011; Rossi et al. 2012; Perley et al. 2013, 2015).

Additionally, using a 2-sided Kolmogorov-Smirnov test (KS-test), we can assess the degree to which the null that the two distribution are drawn from the same distribution can be rejected. We show a graphic representation of the test statistics in Fig. 6. We have run the test on whether it can be rejected that the sample criteria is drawn from the same distribution as the *Swift* sample, if the observed sample is dissimilar from the statistical sample, and again whether the observed sample differs from the full *Swift* sample. A high p-value indicates little evidence against the null meaning for the parameters investigated here, only the X-ray derived column densities exhibits the highest degree of dissimilarity, but not to a significant level. A large part of the tension between the two samples in N_H is driven by a small number of low column densities ($\log(N_H) \lesssim 19 \text{cm}^2$) bursts.

We therefore conclude that the sample presented here, to a high degree represents the intrinsic properties of the GRBs in

the full *Swift* sample. (**This doesn't quite feel exhaustive? Is there a better way of addressing the issue of completeness**)

5.3. Properties of rejected triggers

GRB follow-up requires the immediate availability of the telescope in order to successfully carry out spectroscopic observations. Out of the 158 (**Get exact number**) bursts in the statistical sample, 32 (~ 20 percent) (**Get exact number**) have not been observed due to conditions, not relating the GRB or afterglow properties. The reasons includes unavailability of the telescope due to technical maintenance such as mirror re-coating, a visitor rejecting the TOO trigger, or bad weather at the observing site. Because this cut is irrespective of the GRB properties, it is not expected that this should change sample properties. Addressing whether this cut introduces a bias in the followed sample is not trivial, but in terms of intrinsic GRB properties, the sample distributions does not change significantly, as shown in Sect. 5.2. (**Should this be quantified somehow?**)

5.4. Sample darkness

A subset of all GRBs exhibit no detectable or very faint optical afterglow (Groot et al. 1998; Djorgovski et al. 2001; Fynbo et al. 2001), which had been parametrized in term of "darkness" (Jakobsson et al. 2004; van der Horst et al. 2009). The X-ray properties of this subset has previously been investigated (De Pasquale et al. 2003; Fynbo et al. 2009; Melandri et al. 2012), finding a slightly higher X-ray luminosity compared to the optically bright bursts combined with similar prompt characteristics pointing towards a denser circumburst material. This indicates along with investigations of host galaxy extinction (Greiner et al. 2011; Krühler et al. 2011; Hjorth et al. 2012), that the extinction of the optical afterglow is primarily driven by the presence of dust, local to the burst (**Local dust reference**). Because the dust content of a galaxy is correlated with the gas amount (Bohlin et al. 1978; Güver & Özel 2009), we expect the X-ray derived column densities for the bursts without an optical afterglow to be higher than the ones without.

For all bursts with follow-up within 100 hours we can calculate the "darkness"-parameter, β_{OX} (Jakobsson et al. 2004; Milvang-Jensen et al. 2012). This required the simultaneous measurement of the X-ray flux density and the optical flux density which is in practice never possible. We use the measured acquisition camera magnitude reported in Tab. 1 to get the optical flux density at the beginning of the spectroscopic integration. Because we know the delay between the follow-up and the *Swift* trigger, we can use the measured XRT burst lightcurve (Evans et al. 2007, 2009)⁷ to infer the corresponding X-ray flux density. This is done by either linearly interpolating between temporally neighboring XRT measurements or by extrapolating the last few X-ray data points to the spectroscopic delay. When the afterglow is not detected in the acquisition camera, an upper limit of > 24 mags is used, which propagates into an upper limit on β_{OX} .

In Fig. 7 we compare the $\beta_{OX} - N_H$ distribution with the one presented in Fynbo et al. (2009). We have replaced limits with values, meaning that we artificially bias the distribution towards higher β_{OX} -values because darker bursts naturally fainter in the optical making the fraction of non-detections higher for lower β_{OX} . We marginally confirm the result by Fynbo et al. (2009) that dark bursts $\beta_{OX} < 0.5$ have slightly higher X-ray derived column densities, by calculating the median, 14th, and 86th per-

⁶ http://swift.gsfc.nasa.gov/archive/grb_table/

⁷ http://www.swift.ac.uk/xrt_curves/trigger_numer/flux.qdp

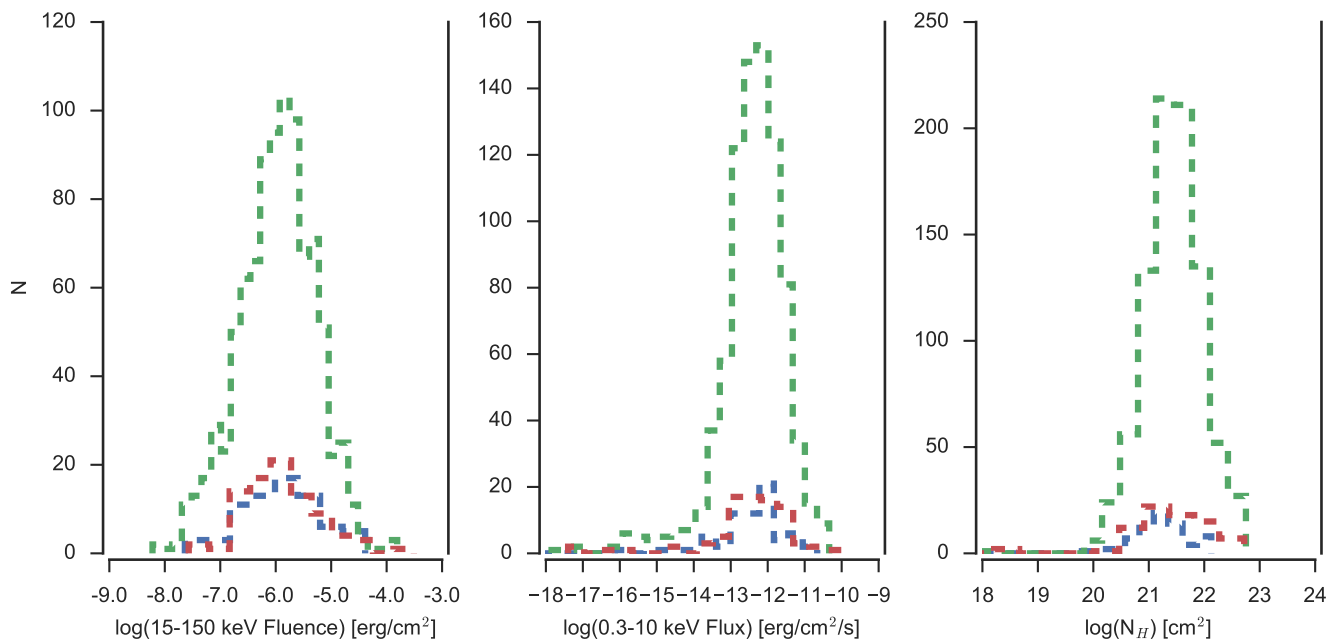


Fig. 5: Comparison between bursts properties of all bursts observed with *Swift*, the properties of the ones that fulfill the sample criteria specified in Sect. 2.1, and the subset that has been observed as part of the statistical sample. The left plot shows the fluence in 15-150 keV as observed by BAT. The middle panel shows the 0.3 - 10 keV flux, 11 hours after the bursts as measured by XRT. Based on the XRT spectrum, (Evans et al. 2009), a hydrogen column density has been inferred which we show in the right most panel.

	Full <i>Swift</i> sample	Statistical sample	Followed up bursts
N_{BAT}	915	71	85
$\log(15 - 150\text{keV fluence})$	$-5.9^{+0.6}_{-0.7}$	$-5.9^{+0.7}_{-0.6}$	$-5.9^{+0.7}_{-0.6}$
N_{XRT}	850	70	84
$\log(0.3 - 10\text{keV flux})$	$-12.3^{+0.7}_{-0.8}$	$-12.3^{+0.4}_{-1.1}$	$-12.4^{+0.8}_{-0.6}$
N_{HI}	878	70	85
$\log(N_H)$	$21.4^{+0.5}_{-0.5}$	$-21.2^{+0.5}_{-0.4}$	$21.4^{+0.7}_{-0.7}$

Table 2: Population properties for the *Swift* sample and the subset of bursts fulfilling the sample criteria. The population characteristics for the three samples exhibit a large degree of similarity, signifying the ability of our selection criteria to effectively capture the underlying population.

centile of the distributions arising by separating the sample at $\beta_{OX} = 0.5$. For bursts with $\beta_{OX} \geq 0.5$ we find $\log(N_H) = 21.4^{+0.7}_{-1.0}$, whereas for $\beta_{OX} < 0.5$ we find $21.8^{+0.5}_{-0.9}$, meaning that the median value for dark bursts is higher, but with a great deal of overlap. A 2-sided KS test fails to reject the null that they are drawn from the same distribution with $p = 0.43$, meaning there is no clear evidence for a discrepancy.

Because we only follow up targets with either a clear afterglow or counterpart, correctly associating a galaxy with a burst when there is no detected optical afterglow is more difficult, see Levesque et al. (2010) and Perley et al. (2017) for a recent example. Because the presence of optical transient is highly dependent on the "darkness", we expect that the β_{OX} sample is biased against dark bursts. The larger relative fraction of upper limits for increased darkness is visible both in the sample presented here and the one in Fynbo et al. (2009). The X-ray properties for the followed sample does not differ significantly from the statistical sample, as shown in Sect. 5.2. Using the table maintained by

Greiner⁸ (How to reference this), we can see how the presence of an optical afterglow affects the follow-up statistics. 50.5 percent of all *Swift*-detected bursts do not have an detected optical afterglow, but this number also includes bursts where no optical telescopes were available, so is a lower limit. For the bursts entering our statistical sample, this number is ~ 27 percent, close to the maximum fraction of dark bursts (Melandri et al. 2012). Of the subsample (3) that have actually been attempted, this number is ~ 18 percent, confirming that we are indeed biased against bursts with an optical afterglow in the spectroscopic sample.

Since *all* GRBs should have an optical afterglow, the presence of an optical afterglow is more a statement about the sensitivity than optical properties of the bursts. (Hmm, how do I finish this?)

⁸ <http://www.mpe.mpg.de/jcg/grbgen.html>

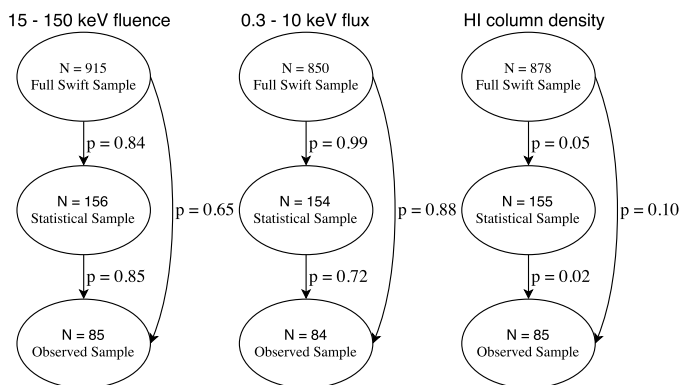


Fig. 6: Relational graph shown the respective p-values that the different sample are drawn from the same underlying distribution. The arrows represent the comparison with each of the p-values are listed next to. Only in the HI column density distribution is there mild evidence against the null, but the discrepancy is mainly driven by a relatively larger fractional contribution from low-column hosts.

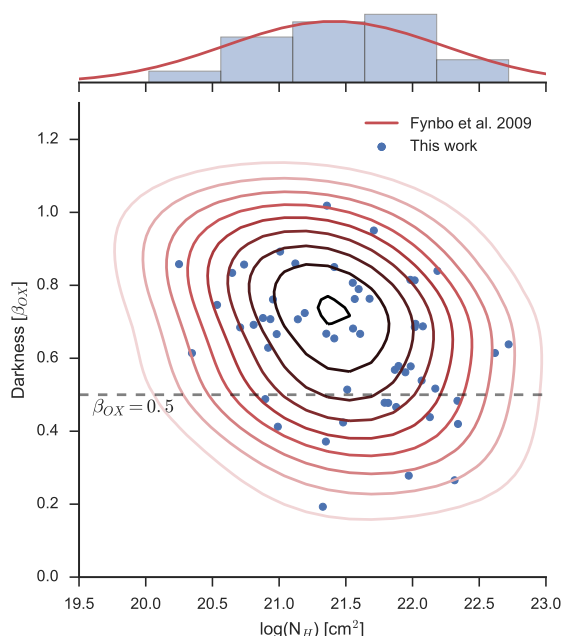


Fig. 7: Optical extinction relative to X-ray against X-ray derived hydrogen column densities. In red is shown the sample presented in Fynbo et al. (2009) where lines indicate the kernel density estimate of the distribution where limits have been replaced with values. Darker colors represented denser points. The corresponding marginal distributions are shown. In blue is the points for the bursts presented here along with the marginal histograms. Limits on β_{OX} is shown by downwards facing arrows.

5.5. On the redshift distribution of GRBs

Because the redshift completeness of our statistical sample is just 54 percent (**Get number**), making inference of the underlying redshift distribution of GRBs on this sample is difficult. Because a large fraction of the bursts for which we were unable to secure a redshift are missing due to terrestrial reasons, see Sect. 5.3, imposing additional unbiasing cuts on the sample can increase the

redshift completeness at the cost of sample size. As long as the cuts we impose are not selective in terms of the burst properties, the sample properties stay the same. The first cut we try is telescope availability such as bad weather, visitor rejected the TOO, or unavailability of the instrument. Because telescope availability is independent on the burst properties, by cutting away these from our sample, the underlying redshift distribution should be conserved. By trimming away the 30 bursts (**Get number**) that can be rejected due to telescope availability, the redshift completeness increases to 63 percent (**Get number**).

As is shown in Sect. 5.1, the redshift completeness decreases with increasing follow-up delay, we can additionally increase the redshift completeness by imposing cuts on the follow-up delay. Our ability to rapidly follow up a burst is also not dependent on the burst properties and therefore we can additionally cut delays longer than 24 hours (all burst in the sample are in principle observable within 24 hours). (**Unfinished section**)

The bias introduced in the redshift distribution by the increased ability to secure redshift of optically brighter bursts has been investigated by Turpin et al. (2016) which find that we systematically find redshift for longer GRBs. Additionally only the brightest GRBs are seen above redshift $z \gtrsim 1$. (**Unfinished section**)

5.6. Hydrogen column densities

Because the locations of GRBs are associated with the most intensely starforming regions (Hogg & Fruchter 1999; Bloom et al. 2002; Fruchter et al. 2006), the GRB afterglow light has to propagate through the large amounts of hydrogen fueling the star formation. Because a significant fraction of the hydrogen has not been ionized yet, the optical depth at the wavelength of $\text{Ly}\alpha$ is very high, saturating at the line center. This causes a strong absorption system to appear in the afterglow continuum. For bursts with $z \gtrsim 1.7$, the position of $\text{Ly}\alpha$ moves into the spectroscopic coverage of X-shooter, meaning that we are able to detect this absorption trough due to $\text{Ly}\alpha$.

Due to the stochastic nature of the $\text{Ly}\alpha$ -forest, the blue wing of the Lyman alpha absorption line is randomly superposed with forest systems, along with strong absorption from Mn II and Si III, making it notoriously difficult to model. Additionally, similarly so, the red wing has got the ISM signatures imprinted on it, especially strong absorption due to Si II, [Si II] and [N V] which can exhibit significant velocity structure. Along with instrumental effects, the generative model for the data that we would use in a likelihood-based analysis would be almost boundless in complexity, making formal fitting of the column densities outside the scope of this paper.

Using an analytic approximation to an absorption line profile and its dependence on the column density (Tepper García 2006), we overplot a synthetic absorption line with a specified column density on our observed spectrum. By tuning the value of the hydrogen column density until the synthetic absorption line matches the spectrum, we can thereby infer the actual column density of the GRB sight line in a manual way. In a similar fashion, the errors on the hydrogen column can be inferred. We show the results of this procedure for all bursts where possible in Fig. 9 and the inferred hydrogen column densities in Tab. 3

In a similar manner to how the X-ray derived column densities was used to assess the sample completeness in Sect. 5.2, we address the same question in terms of the optically derived hydrogen column densities. Using the compilation by ? we have all 81 published HI values previously, we can compare to the 39 new HI columns added by this sample. We note that this sam-

Table 3: Hydrogen column densities for all bursts exhibiting Ly α absorption in the spectral coverage of X-shooter. Corresponding fits are shown in Fig. 9.

GRB	Hydrogen Column
GRB 090809A	21.7 ± 0.2
GRB 090926A	21.55 ± 0.10
GRB 100219A	21.20 ± 0.20
GRB 100425A	21.10 ± 0.20
GRB 100728B	21.2 ± 0.5
GRB 110128A	22.00 ± 0.15
GRB 110818A	21.9 ± 0.4
GRB 111008A	22.40 ± 0.10
GRB 111107A	21.0 ± 0.2
GRB 120119A	22.7 ± 0.2
GRB 120327A	22.0 ± 0.15
GRB 120404A	20.7 ± 0.3
GRB 120712A	19.95 ± 0.15
GRB 120716A	22.00 ± 0.15
GRB 120815A	22.05 ± 0.10
GRB 120909A	21.70 ± 0.10
GRB 121024A	21.85 ± 0.10
GRB 121027A	22.8 ± 0.3
GRB 121201A ^a	22.0 ± 0.3
GRB 121229A	21.7 ± 0.2
GRB 130408A	21.8 ± 0.1
GRB 130427B	21.9 ± 0.3
GRB 130606A	19.91 ± 0.02
GRB 130612A	22.1 ± 0.2
GRB 131011A	22.0 ± 0.3
GRB 131117A	20.0 ± 0.3
GRB 140311A	22.40 ± 0.15
GRB 140430A	21.8 ± 0.3
GRB 140515A	19.0 ± 0.5
GRB 140614A	21.6 ± 0.3
GRB 141028A	20.6 ± 0.15
GRB 141109A	22.1 ± 0.1
GRB 150206A	21.7 ± 0.4
GRB 150403A	21.8 ± 0.2
GRB 150915A ^a	21.2 ± 0.3
GRB 151021A	22.2 ± 0.2
GRB 151027B	20.5 ± 0.2
GRB 160203A	21.75 ± 0.10
GRB 160410A ^b	21.2 ± 0.2
GRB 161014A	21.4 ± 0.3
GRB 161023A	20.96 ± 0.05

Notes. ^(a) Has Ly α emission in the trough. ^(b) Short burst.

ple increase the number of optically derived hydrogen column densities with ~ 50 percent. We compare the median, the 14th, and 86th percentiles of the two distributions where the sample presented here has $21.8_{0.8}^{0.3}$ and the rest of the literature values has $21.5_{1.5}^{0.4}$. We see that the two distribution has a large degree of overlap due to the large width of the distributions, but find a slightly higher median value for the new sample presented here. A 2-sided KS test gets us a p-value of $p = 0.006$, meaning relatively large evidence against the null that the two samples are drawn from the same underlying distribution. Because the bursts that have measurements of the hydrogen column density are selected solely based on our ability to infer a column, it is difficult to make any strong conclusions about the completeness in terms of

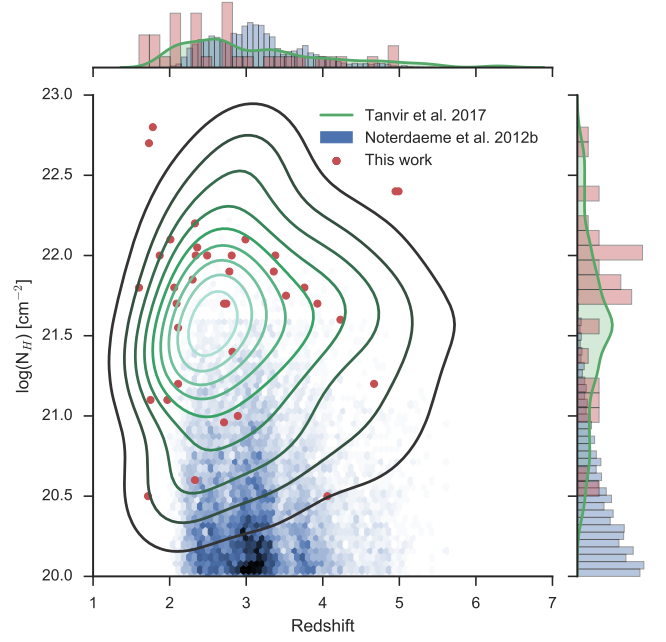


Fig. 8: Distributions of DLA hydrogen column densities for DLAs found in quasar absorption lines, from (Noterdaeme et al. 2012) in blue. Overplot in green is the kernel density estimate is the similar distribution, only for DLAs in GRB sightlines. Values are taken from the compilation in Tanvir2017 et al. (in prep)2, along with the new values presented in this sample. The marginal distributions for the two distribution are also shown, where the different environments probed are clearly visible in the hydrogen column densities, as previously also noted in Fynbo et al. (2009)

gas content. We show the comparison between the two samples in Fig. 8, where we additionally show the column-distribution for 12081 quasar DLAs published in Noterdaeme et al. (2012). The ability of the GRBs to select the highest N_H is immediately visible as is also noted previously (Prochaska et al. 2007; Fynbo et al. 2009). The reason for this is the selection of sight lines as random position of the QSO DLAs whereas the GRB forms in dense regions in the host. The N_H distribution has also be used the infer the position of the gas in host Buchner et al. (2016) where a galaxy-wide gas reservoir is preferred.

6. Discussion

6.1. Comparison to previous samples.

This should also include a discussion of dark bursts. Cuchiara. BAT6 (Salvaterra), TOUGH

7. Conclusion

Acknowledgements. JPUF, BMJ and DX acknowledge support from the ERC-StG grant EGG-278202. The Dark Cosmology Centre is funded by the Danish National Research Foundation. TK acknowledges support by the European Commission under the Marie Curie Intra-European Fellowship Programme in FP7. AdUP acknowledges support by the European Commission under the Marie Curie Career Integration Grant programme (FP7-PEOPLE-2012-CIG 322307). This work made use of data supplied by the UK *Swift* Science Data Centre at the University of Leicester. Finally, we acknowledge expert support from the ESO staff at the Paranal and La Silla observatories in obtaining these target of opportunity data. This work made use of data supplied by the UK *Swift* Science Data Centre at the University of Leicester.

References

- Abbott B. P., et al., 2016, *Phys. Rev. Lett.*, 116, 061102
- Abrarov S. M., Quine B. M., 2015a, *J. Math. Res.*, 7, 44
- Abrarov S. M., Quine B. M., 2015b, *J. Math. Res.*, 7, 163
- Band D. L., 2006, *ApJ*, 644, 378
- Barthelmy S. D., 2000, in AIP Conf. Proc.. AIP, pp 731–735, doi:10.1063/1.1361631, <http://scitation.aip.org/content/aip/proceeding/aipcp/10.1063/1.1361631>
- Barthelmy S. D., et al., 2005, *SSRv*, 120, 143
- Benner D. C., Rinsland C. P., Devi V. M., Smith M. A. H., Atkins D., 1995, *JQSRT*, 53, 705
- Berger E., Fong W., Chornock R., 2013, *ApJ*, 774, L23
- Bloom J. S., Kulkarni S. R., Djorgovski S. G., 2002, *AJ*, 123, 1111
- Bohlin R. C., Savage B. D., Drake J. F., 1978, *ApJ*, 224, 132
- Briggs M. S., et al., 1996, *ApJ*, 459, 40
- Buchner J., Schulze S., Bauer F. E., 2016, *MNRAS*, p. stw2423
- Bufano F., et al., 2012, *ApJ*, 753, 67
- Burrows D. N., et al., 2005, *SSRv*, 120, 165
- Burrows D. N., et al., 2007, in SPIE Conf. Ser.. International Society for Optics and Photonics, p. 668607, doi:10.1117/12.735130
- Cardelli J. a., Clayton G. C., Mathis J. S., 1989, *ApJ*, 345, 245
- Christensen L., Fynbo J. P. U., Prochaska J. X., Thöne C. C., de Ugarte Postigo A., Jakobsson P., 2011, *ApJ*, 727, 73
- Cobb B. E., Bloom J. S., Perley D. A., Morgan A. N., Cenko S. B., Filippenko A. V., 2010, *ApJ*, 718, L150
- Costa E., et al., 1997, *Nature*, 387, 783
- D’Elia V., Stratta G., 2011, *A&A*, 532, A48
- D’Elia V., et al., 2010, *A&A*, 523, A36
- D’Elia V., et al., 2014, *A&A*, 564, A38
- De Pasquale M., et al., 2003, *ApJ*, 592, 1018
- De Ugarte Postigo A., Thöne C. C., Goldoni P., Fynbo J. P. U., 2011, *AN*, 332, 297
- Djorgovski S. G., et al., 1997, *Nature*, 387, 876
- Djorgovski S. G., Frail D. A., Kulkarni S. R., Bloom J. S., Odewahn S. C., Diercks A., 2001, *ApJ*, 562, 654
- Evans P. A., et al., 2007, *A&A*, 469, 379
- Evans P. A., et al., 2009, *MNRAS*, 397, 1177
- Filippenko A. V., 1982, *PASP*, 94, 715
- Fong W., et al., 2013, *ApJ*, 769, 56
- Frail D. A., Kulkarni S. R., Nicastro L., Feroci M., Taylor G. B., 1997, *Nature*, 389, 261
- Freudling W., Romaniello M., Bramich D. M., Ballester P., Forchi V., García-Dabó C. E., Moehler S., Neeser M. J., 2013, *A&A*, 559, A96
- Friis M., et al., 2015, *MNRAS*, 451, 167
- Fruchter A. S., et al., 2006, *Nature*, 441, 463
- Fryer C. L., Heger A., 2005, *ApJ*, 623, 302
- Fynbo J. U., et al., 2001, *A&A*, 369, 373
- Fynbo J. P. U., et al., 2009, *ApJS*, 185, 175
- Fynbo J. P. U., et al., 2014, *A&A*, 12, 1
- Galama T. J., et al., 1998, *Nature*, 395, 670
- Gehrels N., et al., 2004, *ApJ*, 611, 1005
- Gehrels N., Ramirez-Ruiz E., Fox D., 2009, *ARA&A*, 47, 567
- Ginsburg A., et al., 2016, astroquery v0.3.1, doi:10.5281/ZENODO.44961, <https://github.com/astroquery/astroquery>
- Goldoni P., Royer F., François P., Horrobin M., Blanc G., Vernet J., Modigliani A., Larsen J., 2006, *Ground-based Airborne Instrum. Astron. Ed. by McLean*, 6269, 80
- Graff P. B., Lien A. Y., Baker J. G., Sakamoto T., 2016, *ApJ*, 818, 55
- Graham J. F., Fruchter A. S., 2013, *ApJ*, 774, 119
- Greiner J., et al., 2011, *A&A*, 526, A30
- Groot P. J., et al., 1998, *ApJ*, 493, L27
- Güver T., Özel F., 2009, *MNRAS*, 400, 2050
- Hamuy M., Suntzeff N. B., Heathcote S. R., Walker A. R., Gigoux P., Phillips M. M., 1994, *PASP*, 106, 566
- Hartoog O. E., et al., 2013, *MNRAS*, 430, 2739
- Hartoog O. E., et al., 2015, *A&A*, 580, A139
- Hjorth J., et al., 2003, *Nature*, 423, 847
- Hjorth J., et al., 2012, *ApJ*, 756, 187
- Hogg D. W., Fruchter A. S., 1999, *ApJ*, 520, 54
- Horne K., 1986, *PASP*, 98, 609
- Jakobsson P., Hjorth J., Fynbo J. P. U., Watson D., Pedersen K., Björnsson G., Gorosabel J., 2004, *ApJ*, 617, L21
- Jakobsson P., et al., 2006a, *A&A*, 447, 897
- Jakobsson P., et al., 2006b, *A&A*, 460, L13
- Jakobsson P., et al., 2012, *ApJ*, 752, 62
- Jones E., Oliphant T., Peterson P., 2001, SciPy: Open source scientific tools for Python, <http://www.scipy.org/>
- Jones A., Noll S., Kausch W., Szyszka C., Kimeswenger S., 2013, *A&A*, 560, A91
- Kausch W., et al., 2015, *A&A*, 576, A78
- Kocevski D., Petrosian V., 2013, *ApJ*, 765, 116
- Kouveliotou C., Meegan C. A., Fishman G. J., Bhat N. P., Briggs M. S., Koshut T. M., Paciesas W. S., Pendleton G. N., 1993, *ApJ*, 413, L101
- Krühler T., et al., 2011, *A&A*, 534, A108
- Krühler T., et al., 2013, *A&A*, 557, A18
- Krühler T., et al., 2015, *A&A*, 581, A125
- Kumar P., Zhang B., 2015, *Phys. Rep.*, 561, 1
- Letchworth K. L., Benner D. C., 2007, *JQSRT*, 107, 173
- Levan A. J., et al., 2014, *ApJ*, 781, 13
- Levan A., Crowther P., de Grijs R., Langer N., Xu D., Yoon S.-C., 2016, *SSRv*, 202, 33
- Levesque E. M., Kewley L. J., Graham J. F., Fruchter A. S., 2010, *ApJ*, 712, L26
- Lien A., Sakamoto T., Gehrels N., Palmer D. M., Barthelmy S. D., Graziani C., Cannizzo J. K., 2014, *ApJ*, 783, 24
- Lien A., et al., 2016, *ApJ*, 829, 7
- Littlejohns O. M., Tanvir N. R., Willingale R., Evans P. A., O’Brien P. T., Levan A. J., 2013, *MNRAS*, 436, 3640
- L’pez S., et al., 2016, *A&A*, 594, A91
- Melandri A., et al., 2012, *MNRAS*, 421, 1265
- Metzger B. D., et al., 2010, *MNRAS*, 406, 2650
- Milvang-Jensen B., et al., 2012, *ApJ*, 756, 25
- Modigliani A., et al., 2010, *SPIE Astron. Telesc. + Instrum.*, 7737, 773728
- Moffat A. F. J., 1969, *A&A*, 3, 455
- Niino Y., 2011, *MNRAS*, 417, 567
- Noll S., Kausch W., Barden M., Jones A. M., Szyszka C., Kimeswenger S., Vinther J., 2012, *A&A*, 543, A92
- Noterdaeme P., et al., 2012, *A&A*, 547, L1
- Nousek J. A., et al., 2006, *ApJ*, 642, 389
- Pagnini G., Mainardi F., 2010, *JCoAM*, 233, 1590
- Perley D. A., et al., 2009, *AJ*, 138, 1690
- Perley D. A., et al., 2013, *ApJ*, 778, 128
- Perley D. A., et al., 2015, *ApJ*, 801, 102
- Perley D. A., et al., 2016a, *ApJ*, 817, 7
- Perley D. A., et al., 2016b, *ApJ*, 817, 8
- Perley D. A., et al., 2017, *Mon. Not. R. Astron. Soc. Lett.*, 465, L89
- Podsiadlowski P., Ivanova N., Justham S., Rappaport S., 2010, *MNRAS*, 406, no
- Prochaska J. X., Chen H.-W., Dessauges-Zavadsky M., Bloom J. S., 2007, *ApJ*, 666, 267
- Rafelski M., Neeleman M., Fumagalli M., Wolfe A. M., Prochaska J. X., 2014, *ApJ*, 782, L29
- Rossi A., et al., 2012, *A&A*, 545, A77
- Salvaterra R., et al., 2009, *Nature*, 461, 1258
- Salvaterra R., et al., 2012, *ApJ*, 749, 68
- Schlaflly E. F., Finkbeiner D. P., 2011, *ApJ*, 737, 103
- Schlegel D. J., Finkbeiner D. P., Davis M., 1998, *ApJ*, 500, 525
- Schulze S., Malesani D., Cucchiara A., Tanvir N. R., Krühler T., Postigo A. D. U., Leloudas G., 2014, *A&A*, 102, 1
- Selsing J., Fynbo J. P. U., Christensen L., Krogager J.-K., 2015, *A&A*, 87, 14
- Smette A., et al., 2015, *A&A*, 576, A77
- Sparre M., et al., 2011, *ApJ*, 735, L24
- Sparre M., et al., 2014, *ApJ*, 785, 150
- Stanek K. Z., et al., 2003, *ApJ*, 591, L17
- Starling R. L. C., et al., 2011, *MNRAS*, 411, 2792
- Svensson K. M., Levan A. J., Tanvir N. R., Fruchter A. S., Strolger L.-G., 2010, *MNRAS*, 405, 57
- Tanvir N. R., et al., 2009, *Nature*, 461, 1254
- Tanvir N. R., Levan A. J., Fruchter A. S., Hjorth J., Hounsell R. A., Wiersema K., Tunnicliffe R. L., 2013, *Nature*, 500, 547
- Tepper García T., 2006, *MNRAS*, 369, 2025
- Thöne C. C., et al., 2013, *MNRAS*, 428, 3590
- Trujillo I., Aguerri J. A. L., Cepa J., Gutiérrez C. M., 2001, *MNRAS*, 328, 977
- Turpin D., Heussaff V., Dezalay J.-P., Atteia J.-L., Klotz A., Dornic D., 2016, *ApJ*, 831, 28
- Vecchio R. D., Dainotti M. G., Ostrowski M., 2016, *ApJ*, 828, 36
- Vergani S. D., et al., 2011, *A&A*, 535, A127
- Vergani S. D., et al., 2015, *A&A*, 581, A102
- Vernet J., et al., 2009, *Proc. Int. Astron. Union*, 5, 535
- Vernet J., et al., 2011, *A&A*, 536, A105
- Wiersema K., et al., 2012, *MNRAS*, 426, 2
- Wijers R. A. M. J., Bloom J. S., Bagla J. S., Natarajan P., 1998, *MNRAS*, 294, L13
- Woosley S., Bloom J., 2006, *ARA&A*, 44, 507
- Woosley S. E., Heger A., 2006, *ApJ*, 637, 914
- de Ugarte Postigo A., et al., 2010, *A&A*, 513, A42
- van Dokkum P. G., 2001, *PASP*, 113, 1420
- van Paradijs J., et al., 1997, *Nature*, 386, 686
- van der Horst A. J., Kouveliotou C., Gehrels N., Rol E., Wijers R. A. M. J., Cannizzo J. K., Racusin J., Burrows D. N., 2009, *ApJ*, 699, 1087

Table 1: The full sample of afterglows or hosts observed in the program. We here list the burst names and details of the spectroscopic observations. The exposure times and slit widths are given in the order UVB/VIS/NIR. The column Δt shows the time after trigger when the spectroscopic observation was started. Mag_{acq} gives the approximate magnitude (typically in the *R*-band) of the afterglow in the acquisition image.

GRB	Obs Date	Exptime (ks)	Slit width (arcsec)	Airmass	Seeing (arcsec)	Δt (hr)	Mag_{acq}	Redshift	Ref
GRB090313 ^a	2009-03-15	6.9/6.9/6.9	1.0/0.9/0.9	1.2–1.4	1.5	45	21.6	3.3736	(1)
GRB090530 ^a	2009-05-30	4.8/4.8/4.8	1.0/1.2/1.2	1.6–2.2	1.7	20.6	22	1.266	(2)
GRB090809 ^a	2009-08-10	7.2/7.2/7.2	1.0/0.9/0.9	1.2–1.1	1.1	10.2	21	2.737	(2,3)
GRB090926 ^a	2009-09-27	7.2/7.2/7.2	1.0/0.9/0.9	1.4–1.5	0.7	22	17.9	2.1062	(4)
GRB091018	2009-10-18	2.4/2.4/2.4	1.0/0.9/0.9	2.1–1.8	1.0	3.5	19.1	0.9710	(5)
GRB091127	2009-12-02	6.0/6.0/6.0	1.0/0.9/0.9	1.1–1.2	1.0	101	21.2	0.490	(6)
GRB100205A	2010-02-08	10.8/10.8/10.8	1.0/0.9/0.9	1.9–1.8	0.9	71	>24	–	(2)
GRB100219A	2010-02-20	4.8/4.8/4.8	1.0/0.9/0.9	1.3–1.1	0.8	12.5	23	4.667	(7)
GRB100316B	2010-03-16	2.4/2.4/2.4	1.0/0.9/0.9	2.0–2.4	0.6	0.7	18.2	1.18	(2)
GRB100316D-1 ^b	2010-03-17	3.6/3.6/3.6	1.0/0.9/0.9	1.2–1.3	0.8	10	21.5	0.059	(8)
GRB100316D-2	2010-03-19	2.4/2.4/2.4	1.0/0.9/0.9	1.1–1.2	0.9	58	20.2	0.059	(8)
GRB100316D-3	2010-03-20	2.6/2.6/3.2	1.0/0.9/0.9	1.1–1.2	1.1	79	19.9	0.059	(8)
GRB100316D-4	2010-03-21	2.6/2.6/3.2	1.0/0.9/0.9	1.1–1.2	1.5	101	19.9	0.059	(8)
GRB100418A-1	2010-04-19	4.8/4.8/4.8	1.0/0.9/0.9	1.6–1.3	0.7	8.4	18.1	0.624	(9)
GRB100418A-2	2010-04-20	4.8/4.8/4.8	1.0/0.9/0.9	1.2–1.3	0.6	34	19.2	0.624	(9)
GRB100418A-3	2010-04-21	4.8/4.8/4.8	1.0/0.9/0.9	1.2–1.4	0.7	58	>24	0.624	(9)
GRB100424A ^c	2013-03-11	4.8/4.8/4.8	1.0/0.9/0.9	1.1–1.2	0.9	25239.1	>24	2.465	(2)
GRB100425A	2010-04-25	2.4/2.4/2.4	1.0/0.9/0.9	1.5–1.3	0.7	4	20.6	1.755	(2,3)
GRB100615A ^c	2013-03-05	4.8/4.8/4.8	1.0/0.9/0.9	1.0–1.1	0.9	23858.8	>24	1.398	(2)
GRB100621A	2010-06-21	2.4/2.4/2.4	1.0/0.9/0.9	1.3–1.4	1.0	7.1		0.542	(2)
GRB100625A ^{c,f}	2010-07-07	4.8/4.8/4.8	1.0/0.9/0.9	1.1–1.0	0.8	278.7	>24	0.452	(2)
GRB100724A ^{a,d}	2010-07-24	4.2/4.2/4.2	1.0/0.9/0.9	1.5–2.3	0.7	0.2		1.288	(2)
GRB100728B ^e	2010-07-29	7.2/7.2/7.2	1.0/0.9/0.9	1.5–1.1	0.6	22	23	2.106	(2)
GRB100814A-1 ^d	2010-08-14	0.9/0.9/0.9	1.0/0.9/0.9	1.9–1.7	0.5	0.9	19	1.439	(2)
GRB100814A-2	2010-08-14	4.8/4.8/4.8	1.0/0.9/0.9	1.5–1.2	0.7	2.1	19	1.439	(2)
GRB100814A-3	2010-08-18	4.8/4.8/4.8	1.0/0.9/0.9	1.2–1.0	0.6	98	20	1.439	(2)
GRB100816A ^f	2010-08-17	4.8/4.8/4.8	1.0/0.9/0.9	1.8–1.6	0.8	28.4		0.805	(2)
GRB100901A	2010-09-04	2.4/2.4/2.4	1.0/0.9/0.9	1.5–1.5	1.9	66	>24	1.408	(10)
GRB101219A	2010-12-19	7.2/7.2/7.2	1.0/0.9/0.9	1.1–1.7	1.8	3.7		0.718	(2)
GRB101219B-1 ^a	2010-12-20	4.8/4.8/4.8	1.0/0.9/0.9	1.6–2.6	1.4	11.6	20	0.552	(11)
GRB101219B-2 ^a	2011-01-05	7.2/7.2/7.2	1.0/0.9/0.9	1.2–2.0	1.0	394	22.7	0.552	(11)
GRB101219B-3 ^a	2011-01-25	7.2/7.2/7.2	1.0/0.9/0.9	1.4–2.1	0.7	886	>24	0.552	(11)
GRB110128A	2011-01-28	7.2/7.2/7.2	1.0/0.9/0.9	2.0–1.6	0.6	5.5	22.5	2.339	(2)
GRB110407A	2011-04-08	9.6/9.6/9.6	1.0/0.9/0.9	1.4–1.3	2.1	12.4	23	–	(2)
GRB110709B ^c	2013-03-19	7.2/7.2/7.2	1.0/0.9/0.9	1.6–1.1	0.9	14834.8	>24	–	(2)
GRB110715A ^a	2011-07-16	0.6/0.6/0.6	1.0/0.9/0.9	1.1–1.1	1.6	12.3	18.5	0.82	(2)
GRB110721A ^a	2011-07-22	2.4/2.4/2.4	1.0/0.9/0.9	1.2–1.4	2.3	28.7	>24	0.382	(2)
GRB110808A	2011-08-08	2.4/2.4/2.4	1.0/0.9/0.9	1.2–1.1	1.0	3.0	21.2	1.3488	(2)
GRB110818A	2011-08-19	4.8/4.8/4.8	1.0/0.9/0.9	1.3–1.3	0.9	6.2	22.3	3.36	(2)
GRB111005A ^{a,c}	2013-04-01	1.2/1.2/1.2	1.0/0.9/0.9	1.3–1.3	0.7	13052.0	>24	0.013?	(2)
GRB111008A-1	2011-10-09	8.8/8.8/8.4	1.0/0.9/0.9	1.1–1.0	1.3	8.5	21	4.9898	(12)
GRB111008A-2	2011-10-10	8.0/8.0/7.2	1.0/0.9/0.9	1.3–1.0	0.9	20.1	22	4.9898	(12)
GRB111107A	2011-11-07	4.8/4.8/4.8	1.0/0.9/0.9	1.8–1.5	0.8	5.3	21.5	2.893	(2)
GRB111117A ^f	2011-11-19	4.8/4.8/4.8	1.0/0.9/0.9	1.5–1.4	0.7	38	>24	1.3?	(2)
GRB111123A-1	2011-11-24	6.2/6.6/6.6	1.0/0.9/0.9	1.6–1.1	0.8	12.2	>24	3.1516	(2)
GRB111123A-2 ^c	2013-03-07	2.4/2.4/2.4	1.0/0.9/0.9	1.0–1.0	0.5	11266.1	>24	3.1516	(2)
GRB111129A	2011-11-30	3.6/3.6/3.6	1.0/0.9/0.9	1.6–2.1	1.9	8.7		–	(2)
GRB111209A-1	2011-12-10	4.8/4.8/4.8	1.0/0.9/0.9	1.1–1.2	0.8	17.7	20.1	0.677	(13)
GRB111209A-2	2011-12-29	9.6/9.6/9.6	1.0/0.9/0.9	1.2–2.0	1.0	497	23	0.677	(13)
GRB111211A ^a	2011-12-13	2.4/2.4/2.4	1.0/0.9/0.9	1.4–1.6	0.6	31	19.5	0.478	(2)
GRB111228A	2011-12-29	2.4/2.4/2.4	1.0/0.9/0.9	1.4–1.4	0.7	15.9	20.1	0.716	(2)
GRB120118B ^c	2013-02-13	3.6/3.6/3.6	1.0/0.9/0.9	1.1–1.0	0.7	9393.4	>24	2.943	(2)
GRB120119A-1	2012-01-19	2.4/2.4/2.4	1.0/0.9/0.9	1.1–1.1	0.6	1.4	17	1.728	(2)
GRB120119A-2	2012-01-19	1.2/1.2/1.2	1.0/0.9/0.9	1.8–1.9	0.5	4.5	20	1.728	(2)
GRB120119A-3 ^c	2013-02-26	4.8/4.8/4.8	1.0/0.9/0.6JH	1.0–1.1	1.8	9693.9	>24	1.728	(2)
GRB120211A-1 ^c	2013-02-17	4.8/4.8/4.8	1.0/0.9/0.9	1.1–1.4	1.3	8918.7	>24	2.346	(2)

Table 1: The full sample of afterglows or hosts observed in the program (continued).

GRB	Obs Date	Exptime	Slit width	Airmass	Seeing	Δt	Mag _{acq}	Redshift	Ref
		(ks)	(arcsec)		(arcsec)	(hr)			
GRB120211A-2 ^c	2013-03-20	3.6/3.6/3.6	1.0/0.9/0.9	1.1–1.2	1.2	9660.3	>24	2.346	(2)
GRB120224A	2012-02-25	2.4/2.4/2.4	1.0/0.9/0.9	1.7–2.1	1.3	19.8	22.3	1.10	(2)
GRB120311A ^a	2012-03-11	2.4/2.4/2.4	1.0/0.9/0.9	1.6–1.4	0.7	3.7	21.6	0.350	(2)
GRB120327A-1 ^a	2012-03-27	2.4/2.4/2.4	1.0/0.9/0.9	1.6–1.4	0.6	2.1	18.8	2.815	(14)
GRB120327A-2 ^a	2012-03-28	4.2/4.2/4.2	1.0/0.9/0.9	1.0–1.1	0.6	29	22.5	2.815	(14)
GRB120404A	2012-04-05	9.6/9.6/9.6	1.0/0.9/0.9JH	1.7–1.3	1.3	15.7	21.3	2.876	(2)
GRB120422A	2012-04-22	4.8/4.8/4.8	1.0/0.9/0.9	1.3–1.3	0.7	16.5	22	0.283	(15)
GRB120712A	2012-07-13	4.8/4.8/4.8	1.0/0.9/0.9	1.5–2.5	1.5	10.4	21.5	4.175	(2)
GRB120714B	2012-07-15	4.8/4.8/4.8	1.0/0.9/0.9JH	1.5–1.2	1.2	7.8	22.1	0.398	(2)
GRB120716A ^a	2012-07-19	3.6/3.6/3.6	1.0/0.9/0.9JH	1.8–2.6	1.1	62	20.9	2.486	(2)
GRB120722A ^b	2012-07-22	4.8/4.8/4.8	1.0/0.9/0.9	1.3–1.3	1.2	10.3	23.6	0.959	(2)
GRB120805A ^b	2012-08-14	3.6/3.6/3.6	1.0/0.9/0.9JH	1.3–1.7	0.9	218	>24	2.8?	(2)
GRB120815A ^a	2012-08-15	2.4/2.4/2.4	1.0/0.9/0.9	1.3–1.4	0.7	1.69	18.9	2.358	(16)
GRB120909A ^d	2012-09-09	1.2/1.2/1.2	1.0/0.9/0.9	1.6–1.6	1.6	1.7	21	3.929	(2)
GRB120923A	2012-09-23	9.6/9.6/9.6	1.0/0.9/0.9JH	1.2–1.4	1.0	18.5	>24	≥ 8	(2)
GRB121024A	2012-10-24	2.4/2.4/2.4	1.0/0.9/0.9	1.2–1.1	0.6	1.8	20	2.300	(17)
GRB121027A	2012-10-30	8.4/8.4/8.4	1.0/0.9/0.9	1.3–1.3	1.3	69.4	21.15	1.773	(2)
GRB121201A	2012-12-02	4.8/4.8/4.8	1.0/0.9/0.9JH	1.1–1.1	1.1	12.9	23	3.385	(2)
GRB121229A	2012-12-29	4.8/4.8/4.8	1.0/0.9/0.9JH	1.4–1.2	1.5	2	21.5	2.707	(2)
GRB130131B ^c	2013-03-09	7.2/7.2/7.2	1.0/0.9/0.9JH	1.3–1.6	1.1	874.1	>24	2.539	(2)
GRB130408A ^a	2013-04-08	1.2/1.2/1.2	1.0/0.9/0.9	1.0–1.0	0.9	1.9	20	3.758	(2)
GRB130418A	2013-04-18	1.2/1.2/1.2	1.0/0.9/0.9	1.4–1.3	1.2	4.6	18.5	1.218	(2)
GRB130427A	2013-04-28	1.2/1.2/1.2	1.0/0.9/0.9JH	1.8–1.8	0.8	16.5	19	0.340	(18)
GRB130427B	2013-04-28	1.2/1.2/1.2	1.0/0.9/0.9JH	1.2–1.0	1.0	20.3	22.7	2.78	(2)
GRB130603B ^f	2013-06-04	2.4/2.4/2.4	1.0/0.9/0.9	1.4–1.4	1.1	8.2	21.5	0.356	(19)
GRB130606A	2013-06-07	4.2/4.2/4.2	1.0/0.9/0.9JH	1.7–1.9	0.9	7.1	19	5.91	(20)
GRB130612A	2013-06-12	1.2/1.2/1.2	1.0/0.9/0.9	1.3–1.3	1.5	1.1	21.5	2.006	(2)
GRB130615A	2013-06-15	1.2/1.2/1.2	1.0/0.9/0.9	2.1–2.2	1.0	0.8	21	3?	(2)
GRB130701A	2013-07-01	1.2/1.2/1.2	1.0/0.9/0.9JH	2.0–2.0	1.4	5.5	19.9	1.155	(2)
GRB131011A ^a	2013-10-13	4.5/4.5/4.5	1.0/0.9/0.9	1.1–1.1	0.8	34.2	>24	1.874	(2)
GRB131030A	2013-10-31	3.6/3.6/3.6	1.0/0.9/0.9	1.1–1.1	1.1	3.4		1.296	(2)
GRB131103A	2013-11-05	2.4/2.4/2.4	1.0/0.9/0.9JH	1.1–1.1	1.0	5.8	220.48	0.599	(2)
GRB131105A	2013-11-05	4.8/4.8/4.8	1.0/0.9/0.9	1.3–1.4	0.8	1.3	222.4	1.686	(2)
GRB131117A	2013-11-17	4.8/4.8/4.8	1.0/0.9/0.9JH	1.3–1.2	1.7	1.1	220	4.042	(2)
GRB131231A ^a	2014-01-01	2.4/2.4/2.4	1.0/0.9/0.9JH	1.4–1.3	nan	20.2	118.5	0.642	(2)
GRB140114A ^c	2014-03-28	5.4/5.4/5.4	1.0/0.9/0.9JH	1.7–1.7	1.2	1745.7	>24	2.8	(2)
GRB140213A ^a	2014-02-14	1.2/1.2/1.2	1.0/0.9/0.9JH	1.5–1.5	0.7	5.8	119.5	1.208	(2)
GRB140301A	2014-03-02	7.2/7.2/7.2	1.0/0.9/0.9JH	1.1–1.1	0.9	9	223.1	1.416	(2)
GRB140311A ^a	2014-03-13	7.6/6.3/8.4	1.0/0.9/0.9JH	1.2–1.2	0.6	32.5	>24	4.95	(2)
GRB140430A	2014-04-30	1.2/1.2/1.2	1.0/0.9/0.9	2.0–1.8	1.6	2.5	119	1.601	(2)
GRB140506A-1	2014-05-07	4.8/4.8/4.8	1.0/0.9/0.9	1.3–1.4	0.7	8.8	220.9	0.889	(2)
GRB140506A-2	2014-05-08	4.8/4.8/4.8	1.0/0.9/0.9	1.2–1.3	0.7	32.9	- >24	0.889	(2)
GRB140515A	2014-05-16	4.8/4.8/4.8	1.0/0.9/0.9	1.3–1.3	1.4	15.5		6.32	(2)
GRB140614A	2014-06-14	2.4/2.4/2.4	1.0/0.9/0.9	1.8–1.8	0.7	3.8	221.5	4.233	(2)
GRB140622A	2014-06-22	1.2/1.2/1.2	1.0/0.9/0.9	1.4–1.3	1.0	0.8		0.959	(2)
GRB141028A ^a	2014-10-29	2.4/2.4/2.4	1.0/0.9/0.9	1.5–1.4	1.0	15.4	220	2.332	(2)
GRB141031A ^{a c}	2015-01-29	2.4/2.4/2.4	1.0/0.9/0.9	1.2–1.3	0.8	10911.8	>24		(2)
GRB141109A-1	2014-11-09	2.4/2.4/2.4	1.0/0.9/0.9JH	1.5–1.7	0.8	1.9	19.2		(2)
GRB141109A-2	2014-11-10	4.3/4.3/4.5	1.0/0.9/0.9JH	1.7–2.0	0.8	25.4	1	2.993	(2)
GRB150206A	2015-02-07	2.4/2.4/2.4	1.0/0.9/0.9	2.1–1.9	0.8	10	21.9	2.993	(2)
GRB150301B	2015-03-02	3.6/3.6/3.6	1.0/0.9/0.9JH	1.2–1.2	1.1	5.1	2	2.087	(2)
GRB150403A	2015-04-04	2.4/2.4/2.4	1.0/0.9/0.9	1.6–1.7	nan	10.8	19.1	1.5169	(2)
GRB150423A ^{d f}	2015-04-23	4.8/4.8/4.8	1.0/0.9/0.9	2.7–2.4	1.4	0.4	1	2.06	(2)
GRB150428A	2015-04-28	2.4/2.4/2.4	1.0/0.9/0.9JH	1.6–1.5	0.8	3.7		1.394	(2)
GRB150514A ^a	2015-05-15	2.4/2.4/2.4	1.0/0.9/0.9	2.3–2.1	0.9	28.4	19.5		(2)
GRB150518A ^a	2015-05-20	2.4/2.4/2.4	1.0/0.9/0.9JH	1.3–1.3	1.7	30.7	1	0.807	(2)
GRB150616A-1 ^a	2015-06-17	2.4/2.4/2.4	1.0/0.9/0.9	1.4–1.5	0.8	5.7		0.256	(2)
GRB150616A-2 ^{a c}	2015-09-12	2.4/2.4/2.4	1.0/0.9/0.9JH	1.2–1.1	1.2	2091.9	>24		(2)
GRB150727A	2015-07-28	3.6/3.6/2.4	1.0/0.9/0.9JH	1.2–1.2	1.4	5.0		0.313	(2)

Table 1: The full sample of afterglows or hosts observed in the program (continued).

GRB	Obs Date	Exptime	Slit width	Airmass	Seeing	Δt	Mag _{acq}	Redshift	Ref
		(ks)	(arcsec)		(arcsec)	(hr)			
GRB150821A ^d	2015-08-21	2.4/2.4/2.4	1.0/0.9/0.9	2.0–1.8	1.3	0.2	116	0.755	(2)
GRB150910A	2015-09-11	1.8/1.8/1.8	1.0/0.9/0.9JH	1.9–1.9	1.3	20.1		1.359	(2)
GRB150915A	2015-09-16	4.8/4.8/4.8	1.0/0.9/0.9JH	1.1–1.1	1.6	3.3	223	1.968	(2)
GRB151021A ^d	2015-10-21	4.2/4.2/4.2	1.0/0.9/0.9	1.0–1.1	1.4	0.75	118.2	2.33	(2)
GRB151027B	2015-10-28	2.4/2.4/2.4	1.0/0.9/0.9JH	1.5–1.7	1.2	5	220.5	4.063	(2)
GRB151029A	2015-10-29	1.2/1.2/1.2	1.0/0.9/0.9JH	1.9–1.7	1.1	1	220	1.423	(2)
GRB151031A	2015-10-31	4.2/4.2/4.2	1.0/0.9/0.9	1.1–1.1	1.1	0.3	220.4	1.167	(2)
GRB160117B	2016-01-18	4.8/4.8/4.8	1.0/0.9/0.9JH	1.1–1.2	1.1	13.5	221	0.87	(2)
GRB160203A ^d	2016-02-03	6.6/6.6/6.6	1.0/0.9/0.9	1.0–1.8	1.0	0.3	118	3.52	(2)
GRB160228A ^c	2016-03-12	4.8/4.8/4.8	1.0/0.9/0.9JH	1.7–1.7	1.0	295.8	>24	1.64	(2)
GRB160303A ^f	2016-03-04	4.8/4.8/4.8	1.0/0.9/0.9JH	1.6–1.5	0.8	19.1		-	(2)
GRB160314A	2016-03-15	4.8/4.8/4.8	1.0/0.9/0.9JH	1.3–1.3	0.8	13.0		0.726	(2)
GRB160410A ^{d,f}	2016-04-10	1.8/1.8/1.8	1.0/0.9/0.9	2.5–2.3	0.5	0.15	220.3	1.717	(2)
GRB160425A	2016-04-26	4.8/4.8/4.8	1.0/0.9/0.9JH	1.3–1.3	0.5	7.2		0.555	(2)
GRB160625B ^a	2016-06-27	2.4/2.4/2.4	1.0/0.9/0.9JH	1.3–1.3	0.7	30	119.1	1.406	(2)
GRB160804A-1 ^a	2016-08-04	2.4/2.4/2.4	1.0/0.9/0.9JH	1.4–1.3	0.6	22.4	221.2	0.736	(2)
GRB160804A-2 ^{a,c}	2016-08-27	3.6/3.6/3.6	1.0/0.9/0.9JH	1.9–1.8	0.6	574.4	>24	0.736	(2)
GRB161001A	2016-10-01	2.4/2.4/2.4	1.0/0.9/0.9JH	1.2–1.3	0.5	6.1			(2)
GRB161007A ^c	2016-10-14	2.4/2.4/2.4	1.0/0.9/0.9JH	1.6–1.6	0.7	323	>24	???	(2)
GRB161014A	2016-10-15	4.8/4.8/4.8	1.0/0.9/0.9JH	1.1–1.2	0.5	11.6	21.4	2.823	(2)
GRB161023A ^a	2016-10-24	1.2/1.2/1.2	1.0/0.9/0.9JH	1.2–1.2	0.9	3	17.5	2.710	(2)
GRB161117A	2016-11-17	2.4/2.4/2.4	1.0/0.9/0.9	1.8–1.6	2.6	0.73	19	2.823	(2)
GRB161219B	2016-12-21	2.4/2.4/2.4	1.0/0.9/0.9JH	1.1–1.1	0.9	35.7		2.710	(2)

Notes. ^(a) Not part of the statistical sample ^(b) Spectrum dominated by light from the host galaxy ^(c) Spectrum of the host galaxy taken long after the burst ^(d) RRM observation ^(e) ADC malfunction during observation ^(f) Short burst

References. (1) de Ugarte Postigo et al. (2010); (2) This work ; (3) Skuladottir (2010); (4) D’Elia et al. (2010); (5) Wiersema et al. (2012); (6) Vergani et al. (2011); Cobb et al. (2010); (7) Thöne et al. (2013); (8) Bufano et al. (2012) ; (9) De Ugarte Postigo et al. (2011) ; (10) Hartoog et al. (2013); (11) Sparre et al. (2011); (12) Sparre et al. (2014); (13) Levan et al. (2014); (14) D’Elia et al. (2014); (15) Schulze et al. (2014); (16) Krühler et al. (2013); (17) Friis et al. (2015)

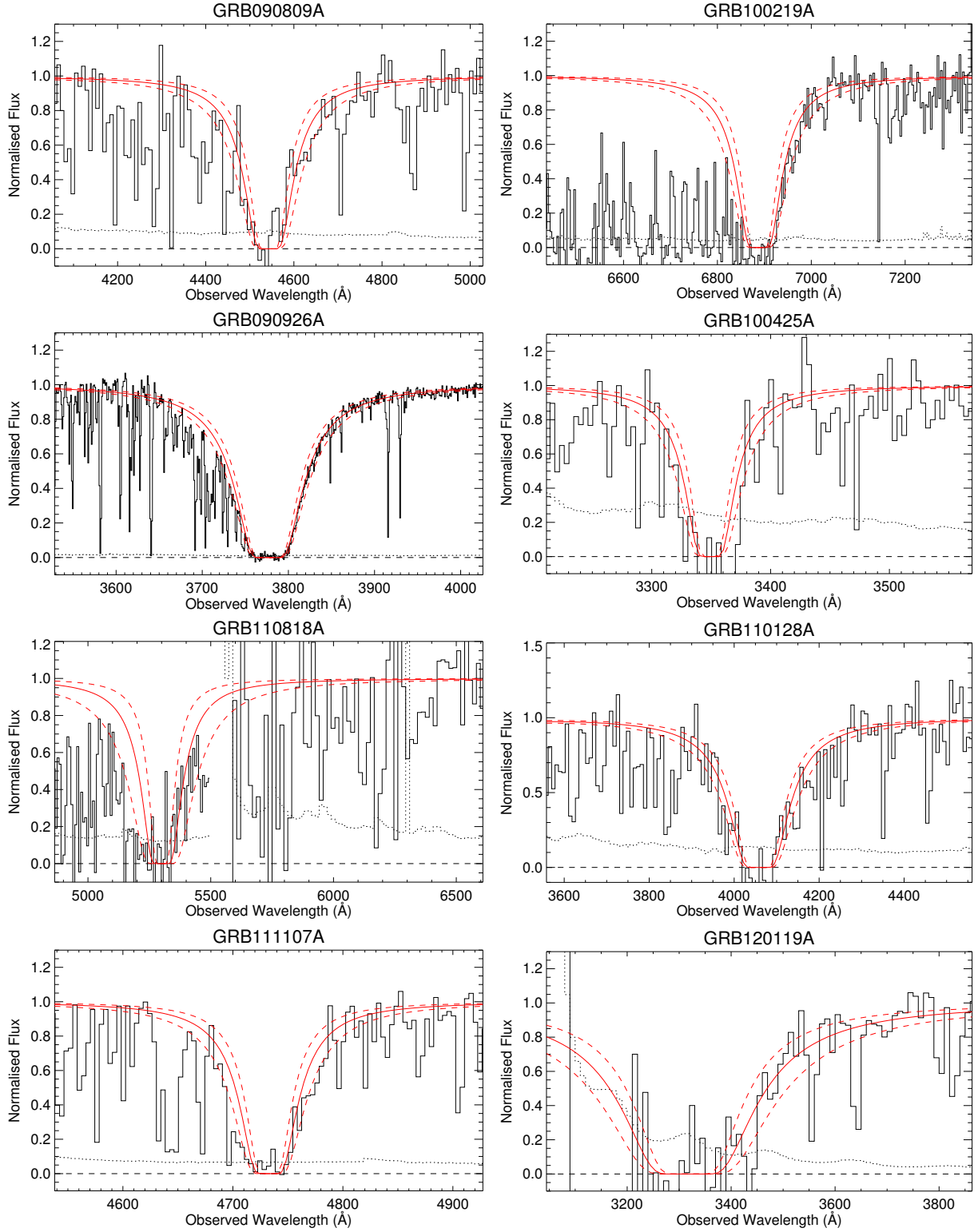


Fig. 9: Measurements of the hydrogen column-densities for all bursts with a clear Lyman alpha absorption system. In solid black is shown the spectrum with black dotted giving the corresponding 1- σ error. Black dashed shows zero flux density. The solid red line is the absorption of column density equal to the value presented in Tab. 3 with the 1- σ interval shown with dashed lines.

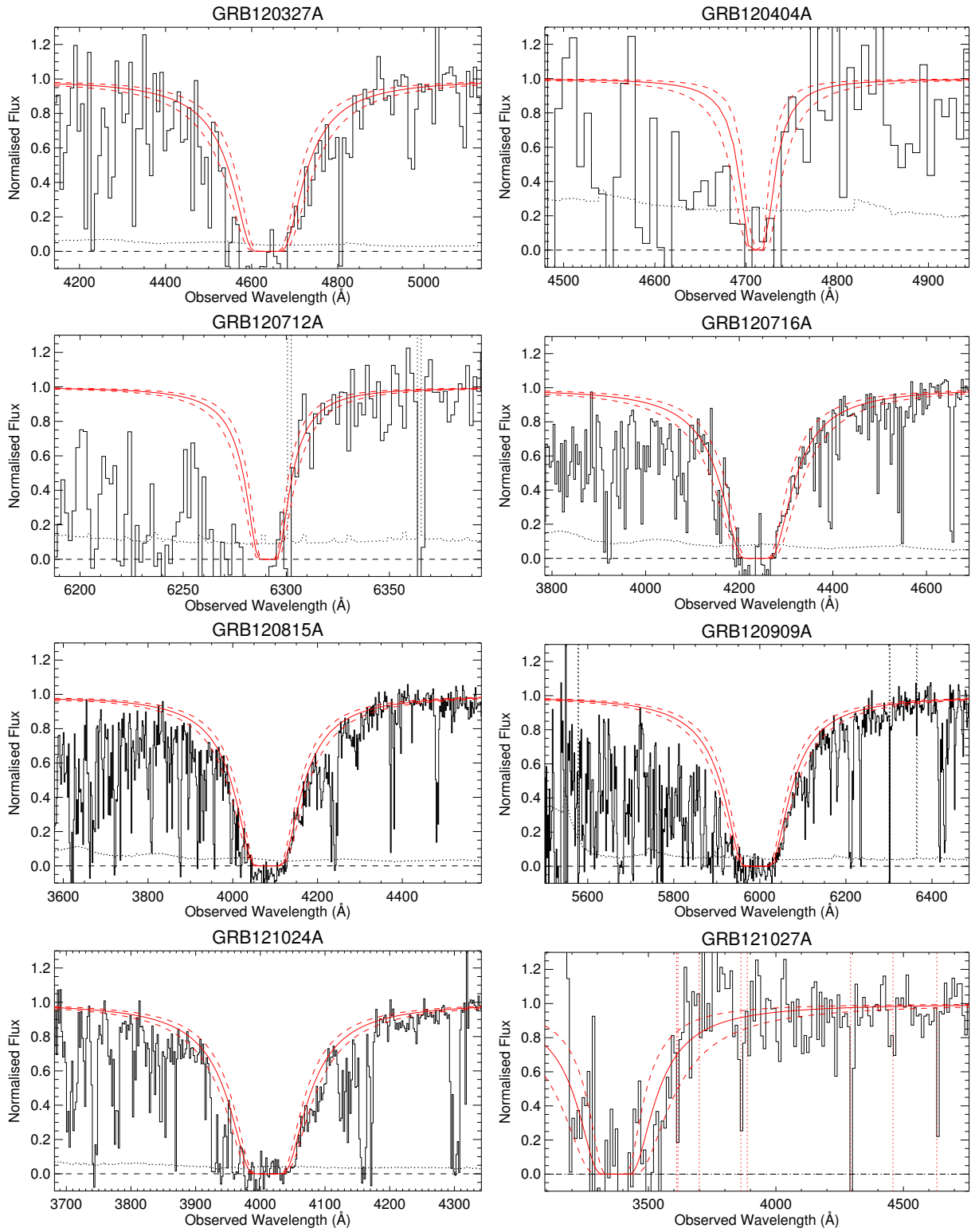


Fig. 9. continued.

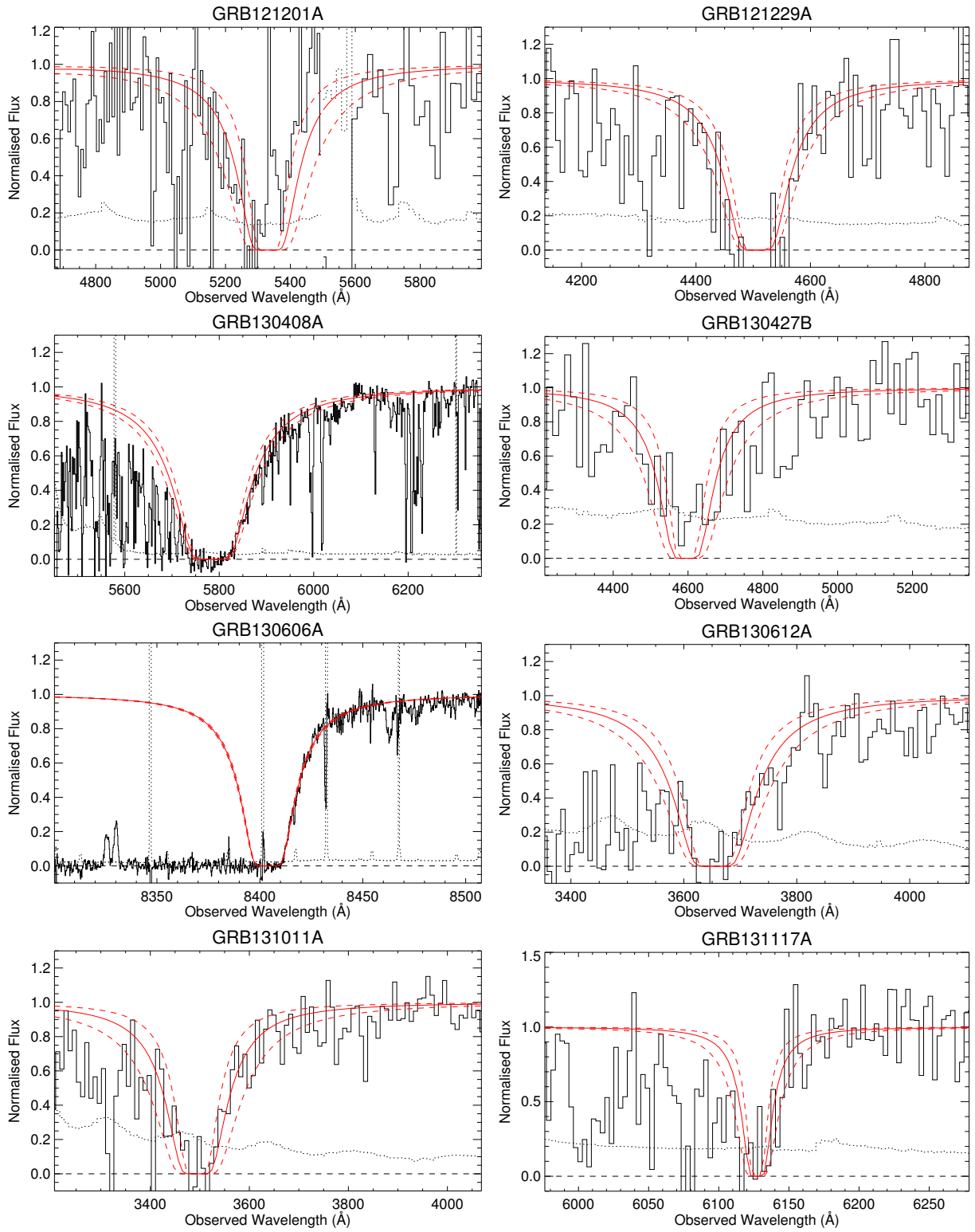


Fig. 9. continued.

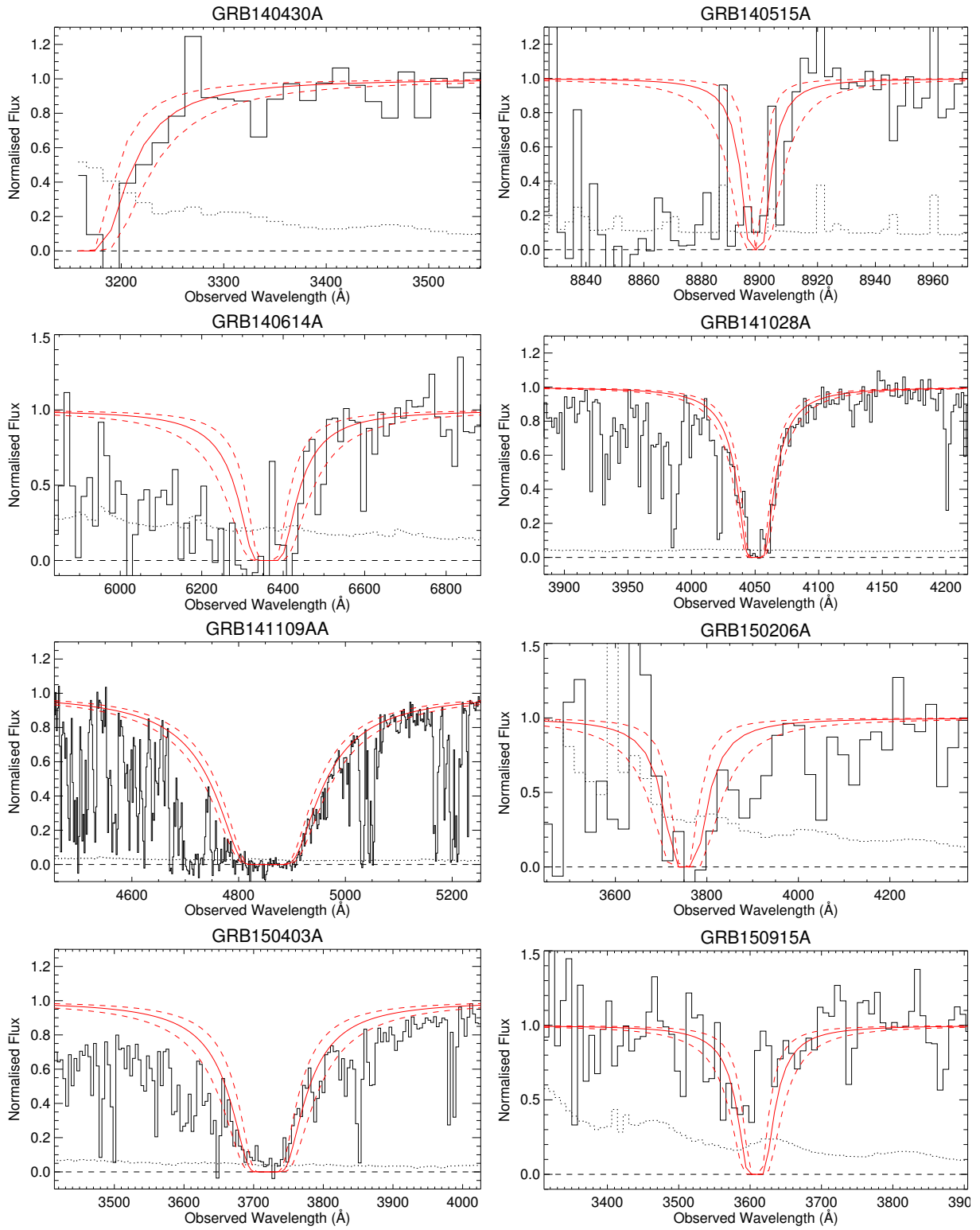


Fig. 9. continued.

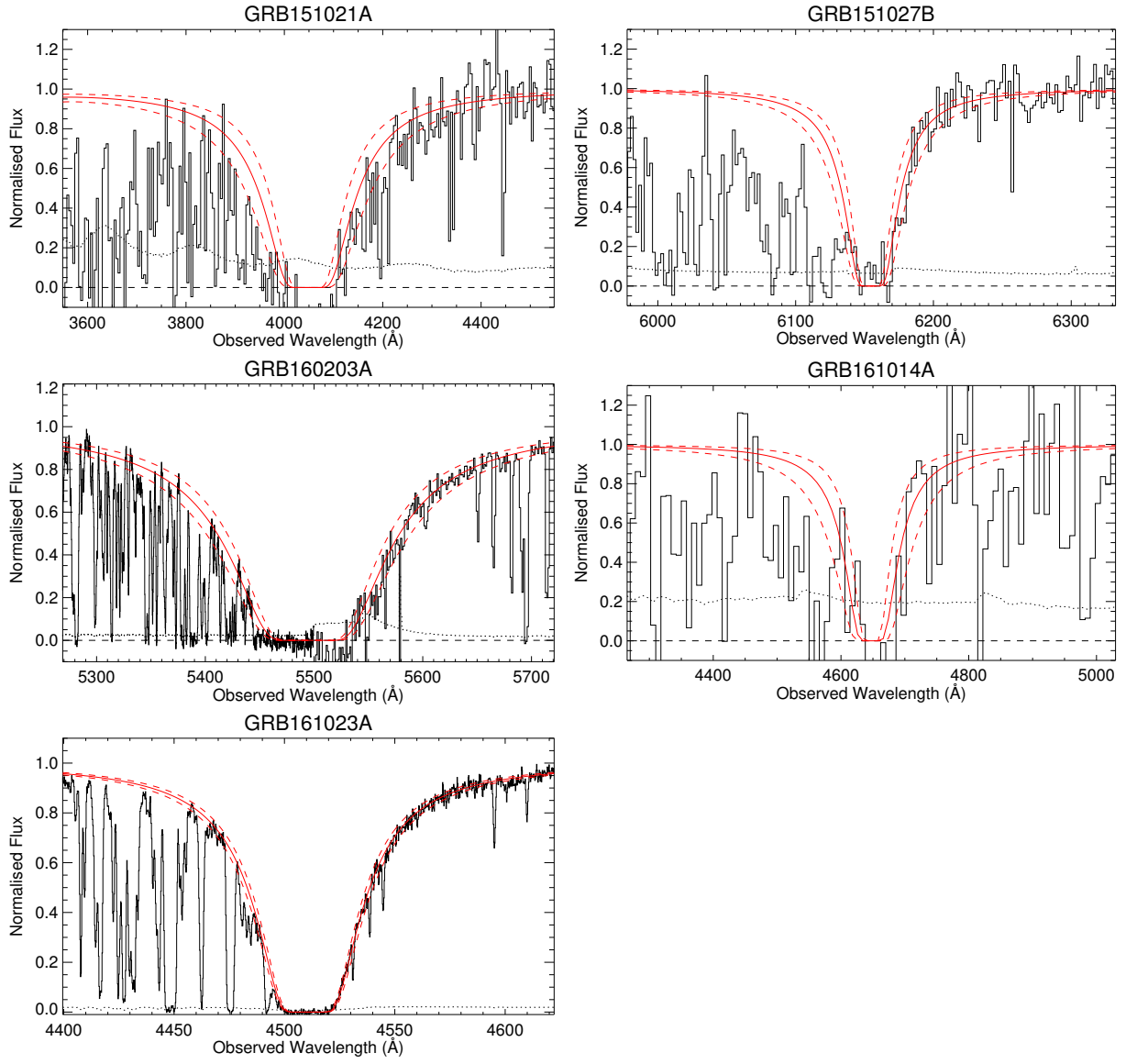


Fig. 9. continued.

Appendix A: The complex error function and the Voigt profile

When modeling the spectral PSF, we need to evaluate the Voigt-profile. The Voigt profile, which is the convolution of the Gaussian and Lorentzian profiles, can, centered at zero, be written as (Pagnini & Mainardi 2010)

$$\begin{aligned} V(\lambda, \sigma, \gamma) &= G(\lambda, \sigma) \otimes L(\lambda, \gamma) \\ &= \int_{-\infty}^{\infty} G(\xi, \sigma) L(\lambda - \xi, \gamma) d\xi \\ &= \int_{-\infty}^{\infty} \frac{1}{\sqrt{2\pi}\sigma} e^{-\left(\frac{\xi}{\sqrt{2}\sigma}\right)^2} \frac{1}{\gamma\pi} \frac{\gamma^2}{(\lambda - \xi)^2 + \gamma^2} d\xi \\ &= \frac{\gamma}{\sqrt{2}\sigma} \frac{1}{\pi^{3/2}} \int_{-\infty}^{\infty} \frac{e^{-\left(\frac{\xi}{\sqrt{2}\sigma}\right)^2}}{(\lambda - \xi)^2 + \gamma^2} d\xi. \end{aligned} \quad (\text{A.1})$$

We can by making the following substitution, $\xi = \sqrt{2}\sigma t$ and $d\xi = \sqrt{2}\sigma dt$, write it as

$$\begin{aligned} V(\lambda, \sigma, \gamma) &= \frac{\sqrt{2}\sigma}{\sqrt{\pi}} \frac{\gamma}{\pi} \int_{-\infty}^{\infty} \frac{e^{-t^2}}{(\lambda - \sqrt{2}\sigma t)^2 + \gamma^2} dt \\ &= \frac{1}{\sqrt{2\pi}\sigma} \frac{\gamma}{\pi} \int_{-\infty}^{\infty} \frac{e^{-t^2}}{\left(\frac{\lambda}{\sqrt{2}\sigma} - t\right)^2 + \left(\frac{\gamma}{\sqrt{2}\sigma}\right)^2} dt. \end{aligned} \quad (\text{A.2})$$

This form of the convolution is closely related to the complex probability function (Letchworth & Benner 2007; Abrarov & Quine 2015a),

$$W(z) = \frac{i}{\pi} \int_{-\infty}^{\infty} \frac{e^{-t^2}}{z - t} dt \quad (\text{A.3})$$

for any complex argument, $z = x + iy$. The complex probability function can be expressed as a sum of a real and imaginary part (Benner et al. 1995; Abrarov & Quine 2015b),

$$\begin{aligned} W(x, y) &= K(x, y) + iL(x, y) \\ &= \frac{y}{\pi} \int_{-\infty}^{\infty} \frac{e^{-t^2}}{(x - t)^2 + y^2} dt + \frac{i}{\pi} \int_{-\infty}^{\infty} \frac{(x - t)e^{-t^2}}{(x - t)^2 + y^2} dt, \end{aligned} \quad (\text{A.4})$$

where is the real part, $\text{Re}[W(x, y)] = \sqrt{2\pi}\sigma V(\lambda, \sigma, \gamma)$ if $x = \frac{\lambda}{\sqrt{2}\sigma}$ and $y = \frac{\gamma}{\sqrt{2}\sigma}$, which can be obtained by using the complex argument, $z = \frac{\lambda + i\gamma}{\sqrt{2}\sigma}$, in the complex probability function. If $\text{Im}[z] \geq 0$, which is always guaranteed for the width of a spectral profile, the complex probability function equals the complex error function. The complex error function has numerous, fast, numerical approximations where in this work we use the `scipy.special.wofz` (Jones et al. 2001) implementation.

Appendix B: Notes on Individual objects

Appendix B.1: GRB090313 ($z = 3.373$)

The first GRB ever observed with X-shooter, during the commissioning of the instrument, this data formed the basis of GCN #9015⁹ and is published in de Ugarte Postigo et al. (2010).

⁹ <http://gcn.gsfc.nasa.gov/gcn3/9015.gcn3>

Due to the lingering brightness of GRB090313, 6.9 ks spectroscopic integration starting 45 hours after the BAT trigger reveals a wealth of absorption features superposed on the afterglow continuum at a common redshift of $z = 3.373$. Two intervening systems at $z = 1.959$ and $z = 1.800$ is identified based on strong Mg II-absorption. Because this burst is observed before the instrument is science-verified, it does not enter into the statistical sample.

Appendix B.2: GRB090530 ($z = 1.266$)

Observed during paranalization of the instrument, this data forms the basis of GCN #15571¹⁰, but is not published elsewhere. Observations began 20.6 hours after the BAT trigger and 4.8 ks spectroscopic integration in all three arms reveals the absorption signature for a host at $z = 1.266$ from the detection of Mg II, Mg I, Si II, Fe II, Al III. Because this burst is observed before the instrument is science-verified, it does not enter into the statistical sample.

Appendix B.3: GRB090809 ($z = 2.737$)

Observed during the first science verification period and was used for GCN #9761¹¹ and is additionally used as the basis for the master thesis by Ása Skúladóttir (2010). 7.2 ks integration starting 10.2 hours after the GRB trigger notice yields the clear afterglow continuum in all arms from with Lyman Limit located in the beginning of the UVB coverage. The simultaneous detection of absorption lines identified as Ly α , Si II, [O I], Si I*, Si IV, C IV, Fe II, Al II, Al III and Mg II at $z = 2.737$ sets it as the redshift of the GRB. Because this burst is observed before the instrument is science-verified, it does not enter into the statistical sample.

Appendix B.4: GRB090926 ($z = 2.106$)

Starting during the second science verification period, this dataset forms the basis of GCN #9942¹² and is additionally published in D'Elia et al. (2010). Spectroscopic integration started 22 hours after the BAT trigger and from the acquisition camera the optical afterglow has $R = 17.9$ mag (vega) at the beginning of the observations which causes a very continuum to be seen in all arms. An absorption trough due to Ly α is clearly visible along with numerous metal resonance lines C IV, Si II, Si I*, Fe II, Mg II, all at $z = 2.106$, marks this as the redshift of the GRB. Because this burst is observed before the instrument is science-verified, it does not enter into the statistical sample.

Appendix B.5: GRB091018 ($z = 0.971$)

The first burst observed during normal operation after science verification was completed and there is the first burst that enter the statistical sample. This data is the basis for GCN # 10042¹³ and is published in Wiersema et al. (2012). With a bright afterglow and a rapid follow-up, this spectrum is of pristine quality. The afterglow continuum is bright throughout all spectroscopic arms which allows the ready detection of Al II, Al III, Fe II, Mn II, Mg II, Mg I, and Ca II located at $z = 0.971$, setting is as the redshift of the host.

¹⁰ <http://gcn.gsfc.nasa.gov/gcn3/15571.gcn3>

¹¹ <http://gcn.gsfc.nasa.gov/gcn3/9761.gcn3>

¹² <http://gcn.gsfc.nasa.gov/gcn3/9942.gcn3>

¹³ <http://gcn.gsfc.nasa.gov/gcn3/10042.gcn3>

Appendix B.6: GRB091127 ($z = 0.490$)

Obtained 4 days after the burst trigger, this data forms the basis for GCN # 10233¹⁴ and is published in Vergani et al. (2011). Due to the late follow-up and a nearby moon, the S/N of the afterglow continuum is poor especially in the UVB arm, why no clear absorption lines are detected against the afterglow continuum, although see Vergani et al. (2011) which report a tentative detection of Mg II. Emission lines from the underlying host is clearly visible with lines from [O II], H β , [O III], and H α all at $z = 0.490$. This bursts is additionally associated with SN2009nz.

Appendix B.7: GRB100205A ($z = na$)

Observed 3 days after the *Swift* trigger. No afterglow or host detected in 10.8 ks. GRB likely located at high redshift¹⁵. The spectrum has not otherwise been published previously.

Appendix B.8: GRB100219A ($z = 4.667$)

The data presented here also formed the basis of GCN # 10441¹⁶ and is published in Thöne et al. (2013). Observations started 12.5 hours after the *Swift* trigger and has a total exposure time of 4.8 ks. Absorption features, including those of Ly α and from a multitude of ions are detected against the afterglow continuum at $z = 4.667$. Additionally, absorption from an intervening system is found at $z = 2.181$.

Appendix B.9: GRB100316B ($z = 1.180$)

The data presented here also formed the basis of GCN # 10495¹⁷. The spectrum has not otherwise been published previously. Observations started 44 minutes after the *Swift* trigger and has a total exposure time of 2.4 ks. Absorption features from Fe II, Al II, Al III, Mg II and Mg I are well detected against the afterglow continuum at $z = 1.180$. Additionally, strong absorption lines from Fe II and Mg II from an intervening system are found at $z = 1.063$.

Appendix B.10: GRB100316D ($z = 0.059$)

The data presented here also formed the basis of GCN # 10512¹⁸, GCN # 10513¹⁹, GCN # 10543²⁰ and is published in Bufano et al. (2012) and Starling et al. (2011). This GRB is very close by and has an associated SN, SN2010bh, and has therefore undergone intense follow-up. The data presented here consists of a subset of the entire VLT/X-shooter campaign, covering the four first observing days while the afterglow still contributes significantly to the total emission. The first observations started 10 hours after the burst, before the SN was discovered, and targeted the star-forming 'A'-region (Starling et al. 2011), not the GRB. A very rich spectrum containing a multitude of emission lines puts the host at $z = 0.059$. For three consecutive nights, 58, 79 and 101 hours after the *Swift* trigger, the afterglow was observed as it transitioned into the spectrum of a high-velocity Ic-BL SN. The observations taken 79 and 101 hours after the burst are taken un-

der programme 084.D-0265(A) (PI: Benetti), but with an identical setup to the first two observations.

Appendix B.11: GRB100418A ($z=0.624$)

The data presented here also formed the basis of GCN # 10620²¹ and GCN # 10631²² and is published in De Ugarte Postigo et al. (2011). The burst have been followed up in three epochs of observations, 0.4, 1.4, and 2.4 days after the burst, each lasting 4.8 ks. The unambiguous redshift of the host, $z = 0.624$, is found from the simultaneous detection of emission features belonging to nebular lines, including H I, [O II], [O III], [Ne III], [N II], [S II], [S III], and [He I] as well as absorption features due to the presence of Zn II, Cr II, Fe II, Mn II, Mg II, Mg I, Ti II, and Ca II, all at a consistent redshift. Temporal evolution of the fine structure lines belonging to Fe II* is found between the epochs.

Appendix B.12: GRB100424A ($z=2.465$)

The data presented here also formed the basis of GCN # 14291²³. The spectrum has not otherwise been published previously. Observations carried out, long after the burst has faded. Emission lines from the host are detected at $z = 2.465$.

Appendix B.13: GRB100425A ($z=1.1755$)

The data presented here also formed the basis of GCN # 10684²⁴ and is used in Skuladottir (2010), but not published elsewhere. Observations started 4 hours after the *Swift* trigger, totaling 2.4 ks. Absorption features from Mg II and Fe II in the afterglow continuum are detected at $z = 1.1755$.

Appendix B.14: GRB100615A ($z=1.398$)

The data presented here also formed the basis of GCN # 14264²⁵, but not published elsewhere. Host observation of a dark burst (D'Elia & Stratta 2011) taken long after the afterglow has faded. Emission lines from the host belonging to [O II], [Ne III], [O III] and H α are detected at a common redshift of $z = 1.398$.

Appendix B.15: GRB100621A ($z=0.542$)

The data presented here also formed the basis of GCN # 10876²⁶, but not published elsewhere. Beginning 7.1 hours after the GRB, 2.4 ks observations reveal emission lines from [O II], H β and [O III] at a common redshift of $z = 0.542$ and a very weak afterglow continuum.

Appendix B.16: GRB100625A ($z=0.452$)

The data presented here is of the candidate host galaxy, taken long after the burst has faded and have not previously been published. 4.8 ks of exposure reveals a weak continuum present in all arms, but an absence of emission lines. This could indicate that the host primarily contains a older stellar population. The redshift, $z = 0.452$, is taken from Fong et al. (2013).

¹⁴ <http://gcn.gsfc.nasa.gov/gcn3/10233.gcn3>

¹⁵ <http://gcn.gsfc.nasa.gov/gcn3/10399.gcn3>

¹⁶ <http://gcn.gsfc.nasa.gov/gcn3/10441.gcn3>

¹⁷ <http://gcn.gsfc.nasa.gov/gcn3/10495.gcn3>

¹⁸ <http://gcn.gsfc.nasa.gov/gcn3/10512.gcn3>

¹⁹ <http://gcn.gsfc.nasa.gov/gcn3/10513.gcn3>

²⁰ <http://gcn.gsfc.nasa.gov/gcn3/10543.gcn3>

²¹ <http://gcn.gsfc.nasa.gov/gcn3/10620.gcn3>

²² <http://gcn.gsfc.nasa.gov/gcn3/10631.gcn3>

²³ <http://gcn.gsfc.nasa.gov/gcn3/14291.gcn3>

²⁴ <http://gcn.gsfc.nasa.gov/gcn3/10684.gcn3>

²⁵ <http://gcn.gsfc.nasa.gov/gcn3/14264.gcn3>

²⁶ <http://gcn.gsfc.nasa.gov/gcn3/10876.gcn3>

Appendix B.17: GRB100724A* ($z = 1.288$)

The data presented here also formed the basis of GCN # 10971²⁷. The spectrum has not otherwise been published previously. The observations were carried out in RRM starting 11 min after the GRB trigger. See section 2.2.1, for a description of the RRM scheme. Absorption lines from several ionic species are detected in the afterglow continuum at a common redshift of $z = 1.288$. This is not a part of the statistical sample.

Appendix B.18: GRB100728B ($z=2.106$)

The data presented here also formed the basis of GCN # 11317²⁸. The spectrum has not otherwise been published previously. Starting 22 hours after the burst trigger, 7.2 ks of observations reveals a faint afterglow continuum with Ly α - and Mg II-absorption at $z = 2.106$. Due to a malfunctioning ADC, the sensitivity of X-shooter is depressed with respect to normal operations, resulting in a poorer throughput. Additionally, the position of the trace on the slit moves due to atmospheric differential refraction.

Appendix B.19: GRB100814A ($z=1.439$)

The spectra presented here has not been published previously. The observations consists of three visits, the first beginning only 0.9 hours after the *Swift* trigger, the other two visits were 2.13 and 98.40 hours after the trigger, respectively. A bright afterglow continuum is present in all visits, allowing identification of absorption features belonging to a wide range of ions at $z = 1.439$. A complex velocity structure in the absorption features belonging to Mg II, shows several components, separated by as much as 500km/s, pointing to a likely merger scenario in the host.

Appendix B.20: GRB100816A ($z=0.805$)

The data presented here also formed the basis of GCN # 11123²⁹. The spectrum has not otherwise been published previously. This short GRB was observed 28.4 hours after the GRB trigger. 4 x 1200 s of exposure reveals two distinct sets of emission lines, spatially offset $\lesssim 1''$, very close in redshift space, $z = 0.8034$ and $z = 0.8049$, indicating either an interacting host or some complex velocity structure of the host. Faint underlying continua are present under both sets of lines.

Appendix B.21: GRB100901A ($z=1.408$)

The data presented here has been published in Hartoog et al. (2013). Because of the unusual lingering brightness of this GRB, 2.4s of observations taken 65.98 hours after the GRB trigger still reveals an afterglow continuum visible across the entire spectral coverage of X-shooter. Absorption lines from a wide range ion put the redshift at $z = 1.408$, with intervening absorption systems at $z = 1.3147$ and $z = 1.3179$.

Appendix B.22: GRB101219A ($z=0.718$)

This data has not been published before. Starting 3.7 hours after the GRB trigger, 7.2 ks of exposure time reveals a very faint continuum in the visual and near-infrared, only visible when heavily

binning the images. No redshift estimate is available from these observations. Late-time Gemini-North observations reveal emission lines from the host at $z = 0.718$ ³⁰.

Appendix B.23: GRB101219B ($z=0.552$)

The data presented here also formed the basis of GCN # 11579³¹ and is published in Sparre et al. (2011). The first observation, taken 11.6 hours after the burst trigger and lasting 4.8ks, reveals absorption from Mg II and Mg I in the host located at $z = 0.552$ on a featureless continuum visible across the entire coverage of X-shooter. Subsequent observations taken 16 and 37 days after the trigger shows the fading spectral signature of a SN, SN2010ma.

Appendix B.24: GRB110128A ($z=2.339$)**Appendix B.25: GRB110407A ($z=na$)****Appendix B.26: GRB110709B ($z=2.1092$ (NEW!!!!))**

This is a late-time observation (> 1 year) and has previously been used in Perley et al. (2016a). In this reduction of the 7.2 ks spectroscopic integration, the tentative detection of [O III] reported in Perley et al. (2016a) is confirmed along with low-significance detection of H α at the end of the spectral coverage, both at a consistent redshift, $z = 2.1092$, securing it as the redshift of the GRB.

Appendix B.27: GRB110715A ($z=0.82$)**Appendix B.28: GRB110721A ($z=0.382$)****Appendix B.29: GRB110808A ($z=1.348$)****Appendix B.30: GRB110818A ($z=3.36$)****Appendix B.31: GRB111005A ($z=0.013$)****Appendix B.32: GRB111008A ($z=4.989$)****Appendix B.33: GRB111107A ($z=2.893$)****Appendix B.34: GRB111117A ($z=2.211$)****Appendix B.35: GRB111123A ($z=3.151$)****Appendix B.36: GRB111129A ($z=na$)****Appendix B.37: GRB111209A ($z=0.677$)****Appendix B.38: GRB111211A ($z=0.478$)****Appendix B.39: GRB111228A ($z=0.716$)****Appendix B.40: GRB120118B ($z = 2.943$)**

The data presented here also formed the basis of GCN # 14225³², but is not published otherwise. This late-time observation of the host of GRB120118B consists of 3.6 ks exposures and contains emission lines belonging to [O II] and [O III] at $z = 2.943$, suggested to be redshift of the host.

²⁷ <http://gcn.gsfc.nasa.gov/gcn3/10971.gcn3>

²⁸ <http://gcn.gsfc.nasa.gov/gcn3/11317.gcn3>

²⁹ <http://gcn.gsfc.nasa.gov/gcn3/11123.gcn3>

³⁰ <http://gcn.gsfc.nasa.gov/gcn3/11518.gcn3>

³¹ <http://gcn.gsfc.nasa.gov/gcn3/11579.gcn3>

³² <http://gcn.gsfc.nasa.gov/gcn3/14225.gcn3>

Appendix B.41: GRB120119A ($z = 1.728$)

The data presented here has not been published before. Three epochs of observations have been obtained, the first two immediately after the burst, and the last one long after the afterglow had faded. Starting 1.4 hours after the *Swift* trigger, the first epoch contains bright afterglow continuum. Rich in absorption features belonging to a multitude of ions, $z = 1.728$ is estimated for the host with intervening systems at $z = 1.476$, $z = 1.214$, $z = 0.662$ and $z = 0.632$. The second epoch, obtained 4.5 hours after the burst contains the fading afterglow. A third epoch is obtained > 1 year after the GRB in which emission lines from H β and H α are found at the redshift of the host, confirming the association of the absorption line system and the host.

Appendix B.42: GRB120211A ($z = 2.346$)

The data presented here has been published in Krühler et al. (2015). Two observations of the host of GRB120211A has been obtained, starting 2013.02.17, > 1 year after the burst has faded. A redshift for this object has been reported by Krühler et al. (2015) and the features seen by those authors are reproduced in these reductions, confirming $z = 2.346$.

Appendix B.43: GRB120224A ($z = 1.10$ NEW!!!)

The data presented here has formed the basis of GCN # 12991³³, and has also been published in Krühler et al. (2015). Starting 19.8 hours after the GRB trigger, a total exposure time of 2.4 ks reveals a faint continuum, starting at ~ 7000 Å and extending all the way through 25000 Å. We detect a $\sim 2\sigma$ emission line which, if interpreted as H α , gives $z = 1.10$, supporting the redshift reported by Krühler et al. (2015).

Appendix B.44: GRB120311 ($z = 0.350$ NEW!!!)

The data presented here has formed the basis of GCN # 12991³⁴, but is not published otherwise. Starting just before twilight, 3.65 hours after the burst, a faint afterglow continuum is detected at all wavelengths. Due to the faintness of the afterglow, no absorption features are discernible superposed on the continuum. Displaced from the afterglow continuum by $1''.4$, emission lines belonging to H β , [O III] and H α are detected at $z = 0.350$. The line belonging to H α shows some extended emission toward the afterglow continuum. The angular distance between the two sources correspond to a projected distance in the host plane of 6 kpc, posing a potential problem for the host redshift, unless the GRB occurred in a merging system. The extended emission in H α , supports this interpretation. This burst is not apart of the statistical sample.

Appendix B.45: GRB120327A ($z = 2.813$)

The data presented here also formed the basis of GCN # 13134³⁵ and is published in D'Elia et al. (2014). The observation consists of two visits, 2.13 hrs and 29.98 hrs after the burst, with an afterglow continuum visible in all arms for both visits. We detect absorption features from Ly-limit, Ly α , C II/C II*, Si II/Si II*, Al I, Fe II and Mg II are detected at a consistent redshift, $z = 2.813$.

³³ <http://gcn.gsfc.nasa.gov/gcn3/12991.gcn3>

³⁴ <http://gcn.gsfc.nasa.gov/gcn3/12991.gcn3>

³⁵ <http://gcn.gsfc.nasa.gov/gcn3/13134.gcn3>

Appendix B.46: GRB120404A ($z = 2.876$)

The data presented here has formed the basis of GCN # 13227³⁶, but is not published otherwise. 9.6 ks integration, starting 15.7 hours after the *Swift*-trigger reveals a low-intensity afterglow continuum on which absorption from Ly α is detected in two distinct regions at redshifts $z = 2.876$ and $z = .255$. These absorption systems are confirmed by ionic absorption features at both of these redshifts.

Appendix B.47: GRB120422A ($z = 0.283$)

The data presented here also formed the basis of GCN # 13257³⁷ and is published in Schulze et al. (2014). A GRB-SN, this burst has been followed up multiple times. The data presented here only contain the first epoch in which the afterglow is still visible and before the rise of SN2012bz. Starting 16.5 hours after the burst, 4.8 ks integration time captures both the host and the burst in emission. A blue afterglow continuum is detected at all wavelengths covered by X-shooter, on which Mg II absorption at $z = 0.283$ is found. Offset by $1''.75$, the host is clearly detected at a consistent redshift with a rich emission line spectrum, the lines extending towards to burst.

Appendix B.48: GRB120712A ($z = 4.175$)

The data presented here also formed the basis of GCN # 13460³⁸ and is not published elsewhere. 4.8 ks integration time, starting 10.5 hours after the BAT trigger, shows a bright afterglow continuum starting at ~ 4720 Å, signifying the onset of the Lyman alpha forest, for a GRB located at $z = 4.175$. Absorption features from Ly α , Fe II, Mg II and Si II are readily detected at a consistent redshift.

Appendix B.49: GRB120714B ($z = 0.398$)

The data presented here also formed the basis of GCN # 13477³⁹, but is not published elsewhere. Observations of this burst started 7.8 hours after the GRB trigger, lasting 4.8 ks. A continuum is visible across the entire spectral coverage of X-shooter, with both emission lines from [O II], H β , [O III] and H α , as well as absorption from Mg II detected at $z = 0.398$, securely setting it as the redshift of the GRB.

Appendix B.50: GRB120716A ($z = 2.486$)

The data presented here also formed the basis of GCN # 13494⁴⁰, but is not published elsewhere. Despite observations starting 62 hours after the *Swift* trigger and lasting 3.6 ks, a bright afterglow is clearly seen, along with a plethora of absorption features. Absorption of Ly α -photons in the host leaves a broad trough, from which the Lyman alpha forest is visible bluewards, all the way down to the Lyman limit. Metal absorption lines from C II, Si II, [O I], Fe II, C IV, Si IV, including fine structure transitions identified as C II*, Si II*, Fe II* and metastable [Ni II] lines are all detected at $z = 2.486$

³⁶ <http://gcn.gsfc.nasa.gov/gcn3/13227.gcn3>

³⁷ <http://gcn.gsfc.nasa.gov/gcn3/13257.gcn3>

³⁸ <http://gcn.gsfc.nasa.gov/gcn3/13460.gcn3>

³⁹ <http://gcn.gsfc.nasa.gov/gcn3/13477.gcn3>

⁴⁰ <http://gcn.gsfc.nasa.gov/gcn3/13494.gcn3>

Appendix B.51: GRB120722A ($z = 0.959$)

The data presented here also formed the basis of GCN # 13507⁴¹, but is not published elsewhere. On 4.8 ks integration time, starting 10 hours after the burst trigger, the simultaneous detection of absorption features belonging to Mg II and Fe II superposed on a blue continuum, and emission lines from [O II], H γ , H β , [O III] and H α , all at $z = 0.959$, confidently sets it as the redshift of the GRB.

Appendix B.52: GRB120805A ($z \sim 3.9$ NEW!!!)

A separate reduction of this burst has been published in Krühler et al. (2015), but not otherwise. Starting 9 days after the burst trigger, this is host observation and does not contain any afterglow continuum. In 3.6 ks integration time, we detect a faint continuum visible from 4500 Å and all the way through 21000 Å, in contrast to what is found previously. The continuum from 4500 - 6000 Å is detected at very low significance. If the drop at 4500 Å is the Lyman limit, this fits with Lyman alpha at ~ 6000 Å, giving $z \sim 3.9$. The absence of nebular lines if due to [O II] falling in a telluric absorption band and the rest being shifted out of the wavelength coverage.

Appendix B.53: GRB120815A* ($z = 2.358$)

Not a part of the statistical sample, this burst also formed the basis of GCN # 13649⁴² and is published in Krühler et al. (2013). Observations started 1.69 hours after the BAT trigger and consist of 2.4 ks integration. A bright afterglow continuum is detected across the entire spectral coverage of X-shooter, with a multitude of absorption lines superposed. Absorption features from the host at $z = 2.358$ include a DLA as well as metal absorption lines from [N V], [S II], Si II, [O I], C IV, Si IV, Fe II, Al II, Al III, Mn II, Mg II, and Mg I. Additionally fine structure lines from [Ni II] and Fe II are exited local to the GRB. Intervening systems are found at $z = 1.539$, $z = 1.693$, and $z = 2.00$.

Appendix B.54: GRB120909A ($z = 3.929$)

The data presented here has formed the basis of GCN # 13730⁴³, but is not published otherwise. A very rapid follow-up, starting only 1.7 hours after the BAT trigger, this 1.2 ks observation captures a very bright afterglow continuum, starting at 4500 Å, signifying the onset of the Lyman limit for a system at $z = 3.929$. Absorption from high-column density hydrogen leaves very prominent absorption features in the form of Ly α , Ly β , and Ly γ , visible in the Lyman alpha forest. Metal absorption lines arising from Fe II, [Ni II], Si II, [S II], Al II, Al III, C II, [O I], C IV, and Zn II are all detected along with the corresponding fine structure lines from (Fe II)*, Si II*, [O I]*, [O I]*, C II*), securely anchoring the redshift of the host.

Appendix B.55: GRB120923A ($z \gtrsim 8?$)**Appendix B.56: GRB121024A ($z = 2.300$)**

The data presented here also formed the basis of GCN # 13890⁴⁴ and is published in Friis et al. (2015). Also rapid, starting 1.8

hours after the *Swift* trigger, a bright afterglow continuum is visible across all arms. A broad absorption feature from Lyman alpha, along with narrow lines from C IV, Si II, Si IV, Fe II, [S II], and Al II, as well as fine structure lines associated with Si II* are all detected at $z = 2.300$, securely setting it as the redshift of the GRB.

Appendix B.57: GRB121027A ($z = 1.773$)

The data presented here has formed the basis of GCN # 13930⁴⁵, but is not published otherwise. Starting 69.6 hours after the GRB trigger, that we detect the afterglow continuum a so high significance in all arms with 8.4 ks integration, testifies to the brightness of this burst. The concurrent identification of emission lines from [O III] and absorption from C IV, Al II, Al III, Mg I, Mg II, and Fe II, tightly constrains the redshift of the burst to be ($z = 1.773$

Appendix B.58: GRB121201A ($z = 3.385$)**Appendix B.59: GRB121229A ($z = 2.707$)****Appendix B.60: GRB130131B ($z = 2.539$)****Appendix B.61: GRB130408A ($z = 3.758$)**

The data presented here also formed the basis of GCN # 14365⁴⁶. The spectrum has not otherwise been published previously. The observations consists of two 600sec spectra taken 1.9hrs after the burst. We detect absorption features from a wide range of ions. We also detect intervening absorption at $z = 1.255$ and $z = 3.248$.

Appendix B.62: GRB130418A ($z = 1.218$)**Appendix B.63: GRB130427A ($z = 0.34$)****Appendix B.64: GRB130427B ($z = 2.78$)****Appendix B.65: GRB130603B ($z = 0.356$)****Appendix B.66: GRB130606A ($z = 5.913$)**

The data presented here also formed the basis of GCN # 14816⁴⁷ and is published in Hartoog et al. (2015). The observations consists of three 2x600sec visits starting 7.1 hrs after the burst at fairly high airmass. We detect absorption features from a wide range of ions at $z = 5.913$ as well as intervening absorption at $z = 2.3103, 2.5207, 3.4515, 4.4660, 4.5309, 4.5427, 4.6497$ and 4.7244.

⁴¹ <http://gcn.gsfc.nasa.gov/gcn3/13507.gcn3>

⁴² <http://gcn.gsfc.nasa.gov/gcn3/13649.gcn3>

⁴³ <http://gcn.gsfc.nasa.gov/gcn3/13730.gcn3>

⁴⁴ <http://gcn.gsfc.nasa.gov/gcn3/13890.gcn3>

⁴⁵ <http://gcn.gsfc.nasa.gov/gcn3/13930.gcn3>

⁴⁶ <http://gcn.gsfc.nasa.gov/gcn3/14365.gcn3>

⁴⁷ <http://gcn.gsfc.nasa.gov/gcn3/14816.gcn3>

Appendix B.67: GRB130612A ($z = 2.006$)

Appendix B.68: GRB130615A ($z = 3?$)

Appendix B.69: GRB130701A ($z = 1.155$)

Appendix B.70: GRB131011A ($z = 1.874$)

Appendix B.71: GRB131030A ($z = 1.296$)

Appendix B.72: GRB131103A ($z = 0.599$)

Appendix B.73: GRB131105A ($z = 1.686$)

Appendix B.74: GRB131117A ($z = 4.042$)

Appendix B.75: GRB131231A ($z = 0.642$)

Appendix B.76: GRB140114A ($z = \sim 2.8?$)

Appendix B.77: GRB140213A ($z = 1.208$)

Appendix B.78: GRB140301A ($z = 1.416$)

Appendix B.79: GRB140311A ($z = 4.95$)

Appendix B.80: GRB140430A ($z = 1.601$)

Appendix B.81: GRB140506A ($z = 0.889$)

Appendix B.82: GRB140515A ($z = \sim 6.32?$)

Appendix B.83: GRB140614A ($z = 4.233$)

Appendix B.84: GRB140622A ($z = 0.959$)

Appendix B.85: GRB141028A ($z = 2.332$)

Appendix B.86: GRB141031A ($z = na$)

Appendix B.87: GRB141109A ($z = 2.993$)

Appendix B.88: GRB150206A ($z = 2.087$)

Appendix B.89: GRB150301B ($z = 1.517$)

Appendix B.90: GRB150403A ($z = 2.06$)

Appendix B.91: GRB150423A ($z = 1.394$)

Appendix B.92: GRB150428A ($z = na$)

Appendix B.93: GRB150514A ($z = 0.807$)

Appendix B.94: GRB150518A ($z = 0.256$)

Appendix B.95: GRB150616A ($z = 1.188$)

Appendix B.96: GRB150727A ($z = 0.313$)

Appendix B.97: GRB150821A ($z = 0.755$)

Appendix B.98: GRB150831A ($z = na$)

Appendix B.99: GRB150910A ($z = 1.359$)

Appendix B.100: GRB150915A ($z = 1.968$)

Appendix B.101: GRB151021A ($z = 2.330$)

The data presented here also formed the basis of GCN # 18426⁴⁸ and is not published elsewhere. The observation was carried out in RRM starting 44 minutes after the GRB trigger. We detect absorption features from a wide range of ions at $z = 2.330$ as well as intervening absorption at $z = 1.49$.

Appendix B.102: GRB151027B ($z = 4.063$)

Appendix B.103: GRB151029A ($z = 1.423$)

Appendix B.104: GRB151031A ($z = 1.167$)

Appendix B.105: GRB160117B ($z = 0.87$)

Appendix B.106: GRB160203A ($z = 3.517$)

The data presented here also formed the basis of GCN # 18982⁴⁹ and is not published elsewhere. The observation was carried out in RRM starting 18 minutes after the GRB trigger. We detect absorption features from a wide range of ions at $z = 3.517$ as well as intervening absorption at $z = 2.203$.

Appendix B.107: GRB160228A ($z = 1.64$)

Appendix B.108: GRB160303A ($z = na$)

Appendix B.109: GRB160314A ($z = 0.726$)

Appendix B.110: GRB160410A ($z = 1.717$)

Appendix B.111: GRB160425A ($z = 0.555$)

Appendix B.112: GRB160625B ($z = 1.406$)

Appendix B.113: GRB160804A ($z = 0.736$)

The data presented here also formed the basis of GCN # 19773⁵⁰, but is not published elsewhere. Observations started 22.37 hours after the BAT trigger and lasted for 2.4ks. The afterglow continuum is detected across the entire spectral coverage of X-shooter and absorption lines from Mg I, Mg II, Fe II and Al II are found at $z = 0.736$. At the same redshift, emission lines from [O II], [O III], H α , H β , H γ , [N II], [S II], [S III] are found. A second epoch, lasting 3.6ks, is obtained after the afterglow has faded, confirming the emission line detections.

Appendix B.114: GRB161001A ($z = 0.891?$)

Appendix B.115: GRB161007A ($z = 4.6 ???$ NEW!!!)

This data has not been published elsewhere. Observations for GRB161007A started 323 hours after the burst trigger and contains the potential host. 4 x 600 seconds of observations reveals a faint continuum rising abruptly above the noise at ~ 6850 Å and continuing through 21000 Å. A very low significance continuum is detected at shorter wavelengths, down to ~ 6000 Å. If the host is located at $z \sim 4.6$, the drop in continuum flux is the Lyman alpha break and the absence of nebular emission lines is due to [O II] being shifted out of the wavelength coverage. Alternatively, an early-type host at $z = 0.71$ could exhibit the 4000 Å break at 6000 Å, but due to the preference of long-duration GRBs for star-forming galaxies, this is the least likely explanation, why we believe the high- z solution.

Appendix B.116: GRB161014A ($z = 2.823$)

The data presented here also formed the basis of GCN # 20061⁵¹, but is not published elsewhere. Starting 11.6 hours after the GRB trigger, 4.8 ks of integration time captures the afterglow continuum across all three spectroscopic arms. A broad absorption

⁴⁹ <http://gcn.gsfc.nasa.gov/gcn3/18982.gcn3>

⁵⁰ <http://gcn.gsfc.nasa.gov/gcn3/19773.gcn3>

⁵¹ <http://gcn.gsfc.nasa.gov/gcn3/20061.gcn3>

⁴⁸ <http://gcn.gsfc.nasa.gov/gcn3/18982.gcn3>

trough due to Lyman alpha is visible, along with metal absorption features from Mg II, Si II, C II, C IV, Al II, Al III, and Fe II, all at $z = 2.823$. Similar to GRB140506 (Fynbo et al. 2014), a break in the continuum shape is detected bluewards of 6000Å, possibly signifying some anomalous form of extinction.

Appendix B.117: GRB161023A ($z = 2.710$)

Appendix B.118: GRB161117A ($z = 1.549$)